④

AFGL-TR-88-0131

AD-A199 187
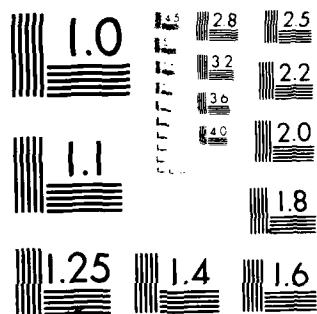
Regional Studies with Broadband Data

Thomas V. McEvilly
Lane R. Johnson

University of California
Geology and Geophysics
Berkeley, CA 94720

15 May 1988

Scientific Report No. 1

DTIC
ELECTE
SEP 0 7 1988
S
E
D

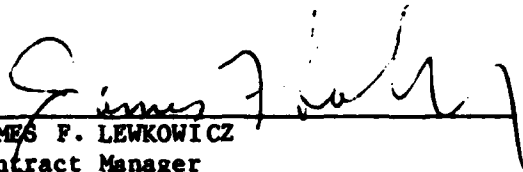88 9 6 149

"This technical report has been reviewed and is approved for publication."

JAMES F. LEWKOWICZ
Contract Manager

HENRY A. OSSING
Chief, Solid Earth Geophysics Branch

FOR THE COMMANDER

DONALD H. ECKHARDT
Director
Earth Sciences Division

ADA199187

REPORT DOCUMENTATION PAGE

1a. REPORT SECURITY CLASSIFICATION	1b. RESTRICTIVE MARKINGS
Unclassified	

2a. SECURITY CLASSIFICATION AUTHORITY	3. DISTRIBUTION/AVAILABILITY OF REPORT
	Approved for public release
2b. DECLASSIFICATION/DOWNGRADING SCHEDULE	Distribution unlimited

4. PERFORMING ORGANIZATION REPORT NUMBER(S)	5. MONITORING ORGANIZATION REPORT NUMBER(S)
	AFGL-TR-88-0131

6a. NAME OF PERFORMING ORGANIZATION	6b. OFFICE SYMBOL (If applicable)	7a. NAME OF MONITORING ORGANIZATION
University of California		Air Force Geophysics Laboratory

6c. ADDRESS (City, State and ZIP Code)	7b. ADDRESS (City, State and ZIP Code)
Geology and Geophysics	Hanscom Air Force Base
University of California	Massachusetts 01731-5000
Berkeley, California 94720	

8a. NAME OF FUNDING/SPONSORING ORGANIZATION	8b. OFFICE SYMBOL (If applicable)	9. PROCUREMENT INSTRUMENT IDENTIFICATION NUMBER
DARPA	DARPA/GSD	F19628-87-K-0032

8c. ADDRESS (City, State and ZIP Code)	10. SOURCE OF FUNDING NOS.			
1400 Wilson Boulevard	PROGRAM ELEMENT NO	PROJECT NO.	TASK NO.	WORK UNIT NO.
Arlington, Virginia 22209				
11. TITLE (Include Security Classification)	61101E	7A10	DA	CD
Regional Studies with Broadband Data				

12. PERSONAL AUTHOR(S)
McEvilly, Thomas V., Johnson, Lane R.

13a. TYPE OF REPORT	13b. TIME COVERED	14. DATE OF REPORT (Yr., Mo., Day)	15. PAGE COUNT
Scientific No. 1	FROM 3/6/87 TO 3/5/88	1988 May 15	94

16. SUPPLEMENTARY NOTATION

17.	COSATI CODES		18. SUBJECT TERMS (Continue on reverse if necessary and identify by block number)
FIELD	GROUP	SUB GR	explosions, earthquakes, moment tensor

19. ABSTRACT (Continue on reverse if necessary and identify by block number)

This report contains the results of two different studies which investigated the use of the second-order moment tensor to represent the properties of seismic sources.

In the first study a new approach to the inversion of body-waveform data for the time-varying moment tensor is developed. The method produces the source model which minimizes the modulus squared of any linear combination of moment tensor components, subject to the constraint that the data are satisfied within specified confidence intervals. This method allows the determination of possible source models other than the least squares solution, enabling one to determine the significance of certain moment tensor properties, for example, the presence or absence of a volume change (isotropic component) in the source. Synthetic tests were used to examine the effect of microseismic noise and lateral heterogeneity on the extreme models of the isotropic component. The method was tested by using long-period waveforms from the Global Digital Seismic Network to estimate the isotropic part of the moment tensor of a

20. DISTRIBUTION/AVAILABILITY OF ABSTRACT	21. ABSTRACT SECURITY CLASSIFICATION
UNCLASSIFIED/UNLIMITED ☒ SAME AS RPT ☐ DTIC USERS ☐	Unclassified

22a. NAME OF RESPONSIBLE INDIVIDUAL	22b. TELEPHONE NUMBER (Include Area Code)	22c. OFFICE SYMBOL
James F. Lewkowicz	(617) 377-3028	AFGL/LWH

DD FORM 1473, 83 APR EDITION OF 1 JAN 73 IS OBSOLETE.

deep Bonin Islands earthquake. The method was also tested on near source data from the nuclear explosion Harzer.

In the second study an unconstrained moment tensor inversion method was used to investigate microearthquake source properties in the Geysers geothermal field in northern California. Improved waveform focal mechanism resolution was a direct consequence of using P and S-wave data together in a progressive velocity-hypocenter inversion to minimize Green function errors. The effects of hypocenter mislocation and velocity model Green function errors on moment tensor estimates were also investigated. In spite of unfavorable recording geometries and large station elevation differences, the results indicate that waveform moment tensor estimates for microearthquake sources can be robust and constrain source mechanisms using data from a relatively small number of stations.

Accession For	
NTIS GRA&I	☒
DTIC TAB	☐
Unannounced	☐
Justification	

By	
Distribution/	
Availability Codes	
Dist	Avail and/or Special
A-1	

DTIC
COPY
INSPECTED
1

TABLE OF CONTENTS

Inversion of Waveforms for Extreme Source Models with an Application to the Isotropic Moment Tensor Component

D. W. Vasco *
L. R. Johnson
Center for Computational Seismology
Lawrence Berkeley Laboratory
and
Department of Geology and Geophysics
University of California
Berkeley, CA 94720

Abstract

We have developed a new approach to the inversion of waveform data for the time-varying moment tensor. The method produces the source model which minimizes the modulus squared of any linear combination of moment tensor components, subject to the constraint that the data are satisfied within specified confidence intervals. This method allows the determination of possible source models other than the least squares solution, enabling one to determine the significance of certain moment tensor properties, for example, the presence or absence of a volume change (isotropic component) in the source. Synthetic tests were used to examine the effect of microseismic noise and lateral heterogeneity on the extreme models of the isotropic component. Lateral heterogeneity is found 'o have a strong effect on the estimation of the isotropic component of the moment tensor.

The method was tested by using long-period waveforms from the Global Digital Seismic Network to estimate the isotropic part of the moment tensor of a deep Bonin Islands earthquake. Modelling indicates that more than 10% of the mechanism might have to be isotropic for detection of volume change in the presence of 10% random noise and only 2% lateral heterogeneity. The least-squares solution indicates that a relatively large change in volume was involved in the source mechanism. However, the minimum extreme solution shows that this volume change is not actually required by the data and thus may not be significant. The method was also tested on near source data from the nuclear explosion Harzer. In this case, in spite of fairly large error bounds, it can be concluded that the source has a clear explosive component.

*Now at:

Earth Sciences Division
Air Force Geophysics Laboratory
Hanscom Air Force Base, MA 01731

INTRODUCTION

A major problem in seismology is the determination of the nature of seismic sources. The analysis of earthquake waveform data is the chief method of studying the faulting process. Other methods such as deep drilling and surface strain measurements are more expensive and time consuming. Furthermore, they do not offer a dynamic picture of the faulting process. Therefore one must turn to the elastic wave radiation for details of the faulting process. One portion of the seismic spectrum in particular, that occupied by body waves, will be examined in this study of seismic sources. We have chosen body waveforms because of the higher resolution they contain and because of the high quality digital waveforms which are becoming available from global digital networks such as the Global Digital Seismic Network (GDSN). Waveform inversion makes use of the whole seismograms, using all the information contained in the time series.

With few exceptions, most moment tensor inversions of waveforms have relied on some form of least squares to derive a "best fitting" solution (Gilbert and Dziewonski 1975, Gilbert and Buland 1976, McCowen 1976, Kanamori and Given 1981, Stump and Johnson 1977, Dziewonski et al. 1981, and Sipkin 1982). The notable exceptions to this approach are the L_1 minimization of Fitch et al. (1980) and Tanimoto and Kanamori (1986) and the linear programming approach of Julian (1986). In an approach related to the latter paper we put forth an inversion method to examine the range of time-varying moment tensor models which agree, to within specified confidence bounds, with observed body-waveform data. Using this technique it is possible to derive extreme models, that is, models which make some property of the source a minimum or maximum. As will be detailed later, the properties will be in terms of the modulus squared of linear combinations of the moment tensor components. Many properties can be put in the form of a linear combination of moment components. Six examples are given in Julian (1986), these include the explosiveness, thrust-like nature, horizontal extensiveness, and vertical compensated linear vector dipole nature of the source. These properties can be used to answer interesting geophysical questions, for example, to decide if an event is a nuclear explosion rather than an earthquake.

One new feature of our approach is the use of quadratic programming for minimizing the modulus squared of the linear combinations of moment tensor components rather than using linear programming for minimizing a linear combination of the components. Quadratic programming is the minimization or maximization of a quadratic functional subject to linear equality and inequality constraints (Dantzig 1963). This approach was taken because of problems in extending the linear programming approach to waveform inversion. Futhermore, it is difficult to interpret linear combinations of moment tensor components in the complex frequency domain and to transform these properties into the time domain. As will be shown, through the use of Parseval's theorem, properties derived through the quadratic programming approach may be conveniently interpreted in both the frequency domain and

2

the time domain. In addition, the quadratic programming method takes the same order of time as the generalized least squares approach and has proven to be very efficient for waveform inversion. We explicitly solve for the time-varying moment tensor, not assuming a source time function. The use of the time-varying moment tensor is a key feature of the method because it allows for motion over curved and complicated fault surfaces. Multiple rupture events also pose no difficulty in the time-varying formulation.

An application of extreme models, the one principally addressed in this paper, is to determine the significance of the isotropic component in the moment tensor. This has importance in at least two areas: nuclear explosion seismology and the determination of deep and intermediate earthquake mechanisms. Nuclear explosions are known to be mainly dilatational sources. However, because of source complexity and scattering due to lateral heterogeneities, the moment tensor contains non-dilatational components. It is necessary to determine the significance of these other components. Furthermore, extreme models allow the determination of the smallest and the largest explosive solutions. This is useful for the estimation of bounds on yields.

In general, earthquakes are thought to have double couple mechanisms. Occasionally however, investigators describe events which contain non-double couple components such as an isotropic trace (Dziewonski and Gilbert 1974, Silver and Jordan 1982). In particular, deep and intermediate earthquakes in subduction zones may be associated with volume decrease. The very high pressures and the possibility of phase changes make the fault mechanics very difficult to model. Therefore, the nature of the faulting deep within the earth is still an open question. The role of volume change can be addressed by the calculation of extreme models. For example, it is possible to compute the model with the minimum total squared trace amplitude and to compare the trace of this model with the deviatoric component. This gives an indication of the relative volume change associated with the event. The computation of such a model results in a quadratic programming problem as will be shown below.

Method of Inversion

Using the representation theorem for seismic sources, a connection can be made between source parameters and observed displacements in terms of equivalent body forces. This is a force system which would produce displacements of the earth's surface equivalent to that from the true physical situation i.e. a heterogeneous fault system with a non-linear rheology. A general indigenous source can be expressed in terms of equivalent body forces (Backus and Mulcahy, 1976), resulting in the relationship

$$u_k(\mathbf{x}, t) = \int_{-\infty}^{\infty} \int_V G_{ki}(\mathbf{x}, t; \mathbf{r}, \acute{t}) f_i(\mathbf{r}, \acute{t}) dV d\acute{t}$$

where u_k is the kth component of displacement, $G_{ki}(\mathbf{x}, t; \mathbf{r}, \acute{t})$ are the Green functions containing propagation effects, $f_i(\mathbf{r}, \acute{t})$ are the sum of the equivalent body forces, and V is

3

the source region where the $f_i(\mathbf{r}, t)$ are non-zero. The summation convention is assumed for repeated indices. The $G_{ki}(\mathbf{x}, t; \mathbf{r}, t)$ may be expanded in a Taylors series (Stump and Johnson, 1977) about the point $\mathbf{r} = \xi$,

$$G_{ki}(\mathbf{x}, t; \mathbf{r}, t) = \sum_{n=0}^{\infty} \frac{1}{n!}(r_1 - \xi_1)\dots(r_n - \xi_n)G_{ki,j_1\dots j_n}(\mathbf{r}, t; \xi, t)$$

Define the force moment tensor

$$M_{ij_1\dots j_n}(\xi, t) = \int_V (r_{j_1} - \xi_{j_1})\dots(r_{j_n} - \xi_{j_n})f_i(\mathbf{r}, t)dV.$$

and the displacement becomes

$$u_k(x, t) = \sum_{n=1}^{\infty} \frac{1}{n!}G_{ki,j_1\dots j_n}(\mathbf{x}, t; \xi, 0) \times M_{ij_1\dots j_n}(\xi, t)$$

where $\times$ represents a temporal convolution.

If the source dimensions are small compared to the wavelengths of interest, then it is necessary to keep only the term for $n = 1$ in the previous expansion and this results in

$$u_k(\mathbf{x}, t) = G_{ki,j}(\mathbf{x}, t; 0, 0) \times M_{ij}(\mathbf{0}, t) \tag{1}$$

for $\xi = 0$. By Fourier transforming this convolution a matrix equation is derived,

$$u_k(\mathbf{x}, f) = G_{ki,j}(\mathbf{x}, f; \mathbf{0}, 0)M_{ij}(\mathbf{0}, f) \tag{2}$$

for each frequency. It is possible to solve either equation (1) or equation (2) for the moment tensor in the time or frequency domain respectively. In order to solve the time domain equation (1) one may assume a source time function which is the same for all moment tensor components, converting the convolution into a multiplication. Alternatively, the convolution equation may be written as a matrix equation and the resulting large block Toplitz system of equations may be solved by a least square error algorithm (Sipkin 1982).

Another approach, the one taken in this paper, is to work in the frequency domain, solving equation (2). Each component may have an arbitrary source-time function and it is only necessary to solve a much smaller system of equations successively at each frequency of interest. This system of equations may be solved by least squares, minimizing the l^2 norm of the residuals,

$$min[\sum_{k=1}^{K}(u_k - G_{kl}M_l)^2]$$

where l is the index vector (i, j). The total number of station components is denoted by K. The index 1 indicates north while indices 2 and 3 represent east and down respectively. The vector **M** is given by the real and imaginary components of the moment tensor:

$$\begin{pmatrix} reM_{11} \\ imM_{11} \\ reM_{21} \\ imM_{21} \\ reM_{22} \\ imM_{22} \\ reM_{31} \\ imM_{31} \\ reM_{32} \\ imM_{32} \\ reM_{33} \\ imM_{33} \end{pmatrix}$$

This results in the generalized inverse solution which may be written in terms of the singular-valued decomposition. In addition to being a well-known, efficient procedure, this method allows one to form the data and model resolution matrices and the unit covariance matrix (Menke 1984).

It is important to find a "best fitting model" which the least squares solution provides, but it is also useful to use the data to answer more specific geophysical questions. For example, is a pure double-couple source sufficient to satisfy the data, or is some volume change present in the source? To answer such a question it is necessary to find the extremum of a linear combination of the moment tensor components, the sum of the diagonal elements of the moment. Alternatively, one could minimize the modulus squared of this quantity, the approach we advocate. The search for the extrema is subject to the constraint that the data u_k are satisfied within some confidence intervals ϵ_k. Thus we seek

$$min[A_l M_l] \tag{3}$$

or,

$$min[M_m{}^T A_{ml} M_l] \tag{4}$$

subject to

$$u_k - \epsilon_k \leq G_{kl} M_l \leq u_k + \epsilon_k \quad k = 1, K. \tag{5}$$

The A_{ml} matrix is crucial because it defines the properties which will be bounded. By changing the elements of A_{ml} a variety of different source characteristics can be considered: the largest and smallest vertical strike-slip fault source, the most and least thrust-like source,

etc. Table 1 presents the coefficients of the quadratic form (A_{ml} in equation 4) for a number of source properties. By changing the sign of the elements the problem is changed from a minimization to a maximization.

The system of equations and inequalities given above results from the local imposition of error bounds for each constraint equation, that is, the confidence interval for each datum is a strict interval which no datum may exceed. If the data set is large it is unlikely that some intervals will not be exceeded (Oldenberg 1983). As an alternative to this imposition of absolute confidence bounds on the data it is possible to impose a statistical bound. Using this approach, one would require that the i th datum is satisfied within some *unspecified* error bound e_i. Specifically, the sum of the error for each constraint should not exceed some pre-determined value E. Algebraically, instead of the constraints in equation (5) we have,

$$u_k \leq G_{kl}M_l + \epsilon_k \quad k = 1, K$$

$$G_{kl}M_l - \epsilon_k \leq u_k \quad k = 1, K \tag{6}$$

and

$$\sum_{i=1}^{K} e_i + s = E$$

$$\epsilon_k \geq 0 \quad k = 1, K$$

$$s \geq 0$$

The additional constraint has been imposed that all the e_i's and s are always positive. If the errors e_i are independent, normal, random variables, the value of E may be calculated using *a priori* estimates of their mean and standard deviations σ_i (Parker and McNutt 1980). Unfortunately, the statistical parameters of errors associated with waveforms are not known *a priori* In addition to microseismic noise, which may be estimated by pre-event noise samples, there is signal generated noise due to errors in the estimation of the Green function. This noise, in both phase and amplitude, is often more significant than microseismic noise and must be accounted for. We will estimate these bounds by taking the difference between the observed data and data predicted by a model derived by an inversion procedure such as least squares. Another method to estimate errors in the waveforms is through Monte Carlo simulation of data sets. This involves using the least squares solution to generate a data set which is then perturbed by an *a priori* distribution of errors. The statistic of this data set may be computed and used to compute confidence intervals with which to derive extreme models. Unfortunately, present day models of lateral heterogeneity are not adaquate to fully represent the Green function errors.

The algorithm used to minimize equation (3) subject to the constraints of equation (5) or (6) is the well known simplex algorithm for linear programming. To minimize the

Table 1. Coefficients for the quadratic form in equation (4) for a variety of moment tensor properties. The real and imaginary components have identical coefficients

QP Coefficients:

SOURCE	Explosive	Thrust-like	Vertical CLVD	Vertical Strike-Slip
M_{xx}^2	1		1	
M_{yy}^2	1		1	
M_{zz}^2	1	1	4	1
$M_{xx}M_{yy}$	2		2	
$M_{xx}M_{zz}$	2		-4	
$M_{yy}M_{zz}$	2		-4	
M_{xz}^2				1
M_{yz}^2				1
$M_{xx}M_{xz}$				-2
$M_{yz}M_{xx}$				-2
$M_{xx}M_{yz}$				-2

7

quadratic functional in equation (4) subject to the constraints requires quadratic programming (Dantzig 1963). By finding the minimum and maximum of the functional subject to the constraints it is possible to derive bounds on model properties from bounds on the data. This is one method to explore the range of possible models rather than derive a single solution.

As mentioned previously, formulating the problem in terms of the square of the modulus of a linear sum of moment tensor components allows the transition between moment tensor properties in the time and frequency domains. This follows from Parseval's theorem which states that the integral of the square of the modulus of a function is equal to the integral of the square of the modulus of the Fourier transform of the function (Bracewell 1978). If one considers the functional $F(\omega_i) = C_i M_i$, as a finite Fourier transform of the time series $f(t)$, then the square of the modulus of $F(\omega_i)$ may be represented as a quadratic form involving a vector $\mathbf{M}$ composed of the real and imaginary parts of the moment tensor components.

$$F(\omega_i)F(\omega_i)^* = \mathbf{M}^T \mathbf{A} \mathbf{M}. \tag{7}$$

Where $F(\omega_i)^*$ is the complex conjugate of $F(\omega_i)$. Because of Parseval's theorem, the sum of the function in equation (7) over all frequencies has the same value as the sum of the amplitude squared of the time series $f(t)$ over all time. Fortunately, our time series are finite and our seismic spectra are band-limited, due to instrument transfer functions. Hence, the extremum of this sum is the same in the time and frequency domain. Therefore, it is possible to compute the minimum or maximum value of the square of the modulus of any linear combination of moment tensor components in the frequency domain, sum the extreme values over all frequencies, and interpret this directly in the time domain. In what follows we will consider the moment rate tensor rather than the moment tensor. The rate tensor has no static offset and hence returns to zero over time.

Deep Earthquakes

Debate has continued about the presence of an isotropic moment tensor component in deep and intermediate subduction zone earthquakes (Dziewonski and Gilbert 1974, Okal and Geller 1979, Silver and Jordan 1982, Hodder 1984, and Riedesel and Jordan 1985). It seems reasonable to expect subducting regions to be areas of compaction accompanied by dewatering, high fluid pressure, crack closure and phase changes. The essential question is if any of these phase changes are meta-stable. Only then can such reactions produce rapid failure which excites high-frequency waves in the Earth. Recently, high pressure experiments (Kirby 1987, Meade and Jeanloz 1988) have detected shear instabilities associated with phase changes. The most recent work recorded sudden failure and acoustic emissions when simulated ocean lithosphere was subjected to pressures of up to 20 GPa at temperatures below 900 deg K. If such physical processes are occuring they should be seismically detectable.

Some investigators have emphasized the possible trade-off between lateral heterogeneities and a possible isotropic component (Okal and Geller 1979). In addition, source complexity such as curved faults and multiple rupture can give rise to non double-couple moment tensor solutions (Sipkin 1986). The derivation of extremal models for the time-varying moment tensor seems well suited to address the question of the presence of an isotropic moment component, given microseismic noise, complex sources, and lateral heterogeneities.

With this in mind we consider a 467.7 km deep, magnitude 5.6 earthquake near the Bonin Islands recorded by 15 GDSN long period instruments (Figure 1 shows the station distribution). The fifteen stations span a distance range from $38.5°$ to $91.7°$ but have a gap in coverage in the southeast quadrant. Shown in Figure 2 are the 15 long period, vertical GDSN seismograms. The first 256 seconds of the records were used in the inversions. The signal to noise ratio is quite high (consider the pre-event microseismic noise) and the arrivals coherent across the array of stations.

Tests with synthetic data

To illustrate the method and also explore its capabilities, we first consider some tests with synthetic data. We adopt the same number, distribution, and type of stations as for the Bonin Islands earthquake (Figure 1), but assume that the event is at a depth of 467.7 km with the source specified by the time-varying moment rate tensor shown in Figure 3. This is a dip-slip event with a superimposed isotropic component. The body waves from the event (P, pP, and sP) were calculated by the WKBJ method (Chapman, 1978) for a PREM Earth model (Dziewonski and Anderson, 1981) and then low-pass filtered to obtain the vertical-component synthetic seismograms shown in Figure 4. Random noise with an amplitude 10% that of the maximum signal has been added to each seismogram to simulate microseismic noise with a signal-to-noise ratio of 10:1. This example is only intended to simulate microseismic noise which should be uncorrelated for the global station distribution considered. This is not the case with signal generated noise arising from lateral heterogeneities which may be correlated when receiver crustal structures are similar.

We now ask the question, what can be said about the possibility of an isotropic component in the source given the noisy, band-limited seismograms? One way to answer this question is to compute the least-squares solution at each frequency and then Fourier transform the results into the time domain where the moment tensor trace can be computed. Such results are shown in Figure 5 where it can be seen that they do a good job of recovering the known solution of Figure 3. But the question remains, because of the microseismic noise in the seismogram, what is the range of possible moment tensor traces? One way to quantify this is to find the models with the maximum and minimum trace amplitudes squared and still satisfying the data within the errors introduced by the noise. That is, minimize the functional in equation (4) with the elements of the A_{ml} matrix given by the explosive terms in Table 1.

BONIN ISLANDS EVENT

Figure 1. Station distribution of GDSN instruments recording the Bonin Islands earthquake of October 4, 1985. The earthquake epicenter is denoted by a cross at the center of the map and the stations by triangles. The magnitude 5.6 event was at a depth of 467.7 km.
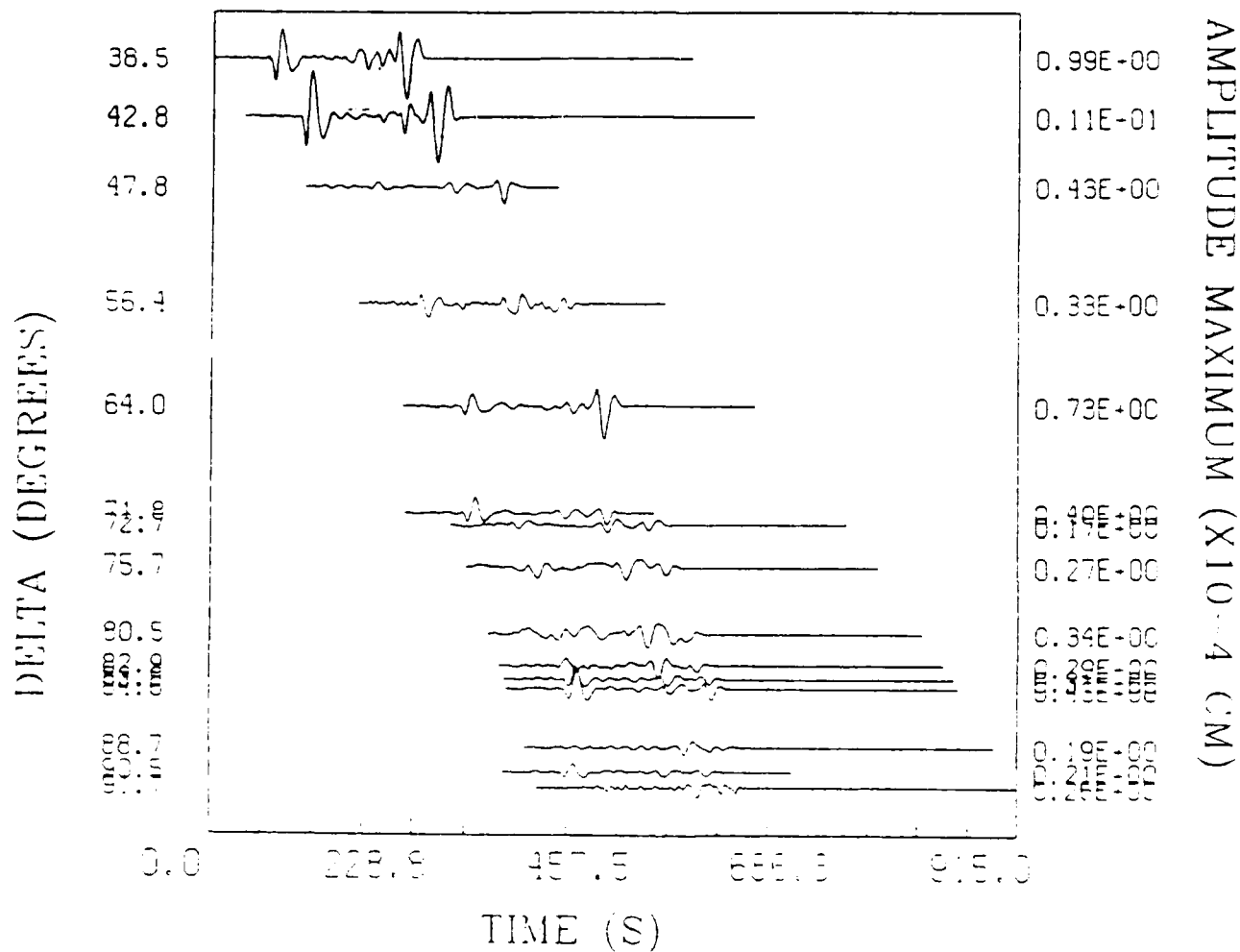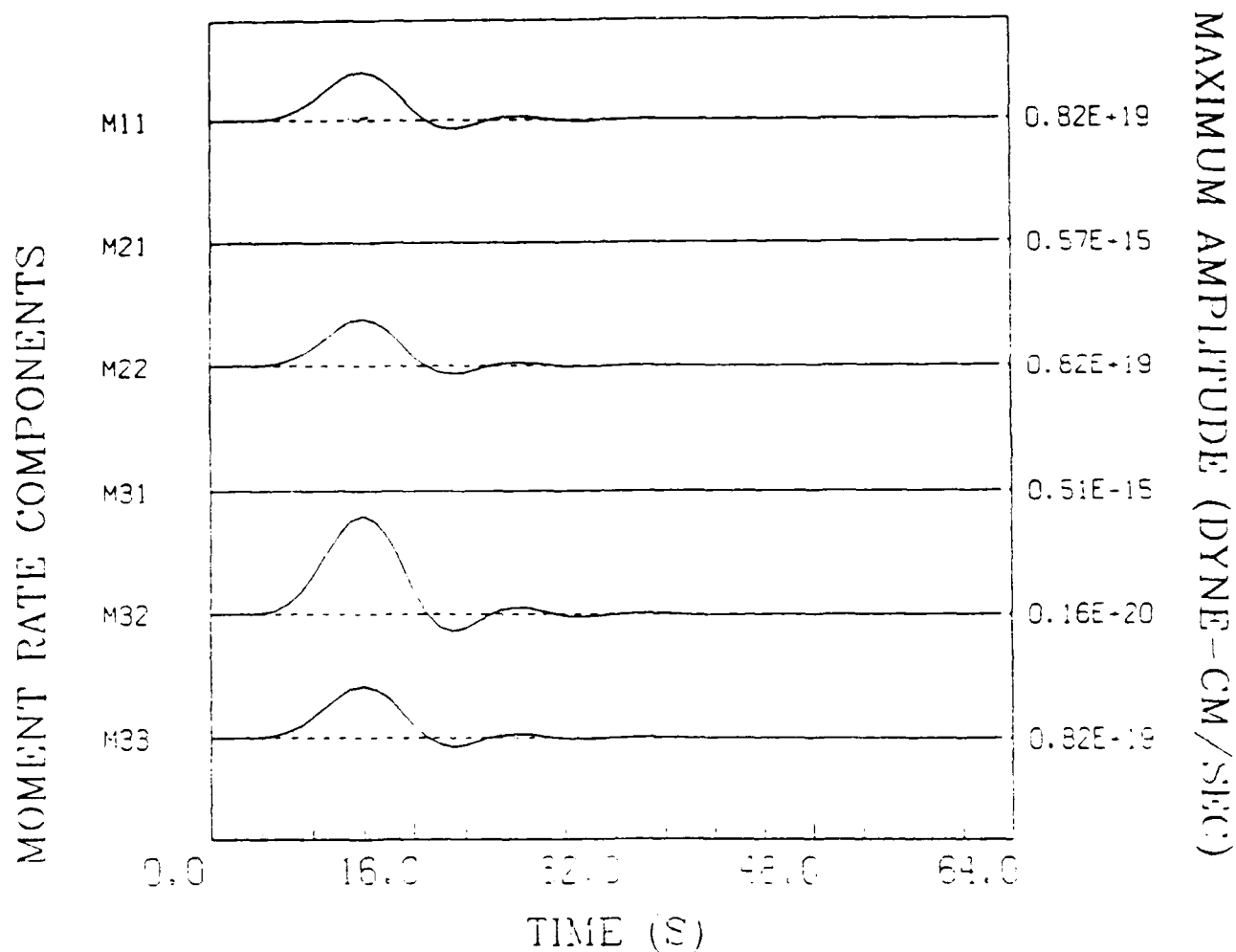
10

Figure 2. GDSN long period seismograms from the Bonin Islands event. The early P arrivals (P, pP, and PP) are present in this section.

11

Figure 3. Moment tensor source used for the synthetic modelling. The source consists of a dip-slip event with a superimposed isotropic component. The isotropic component constituted 60 % of the source.
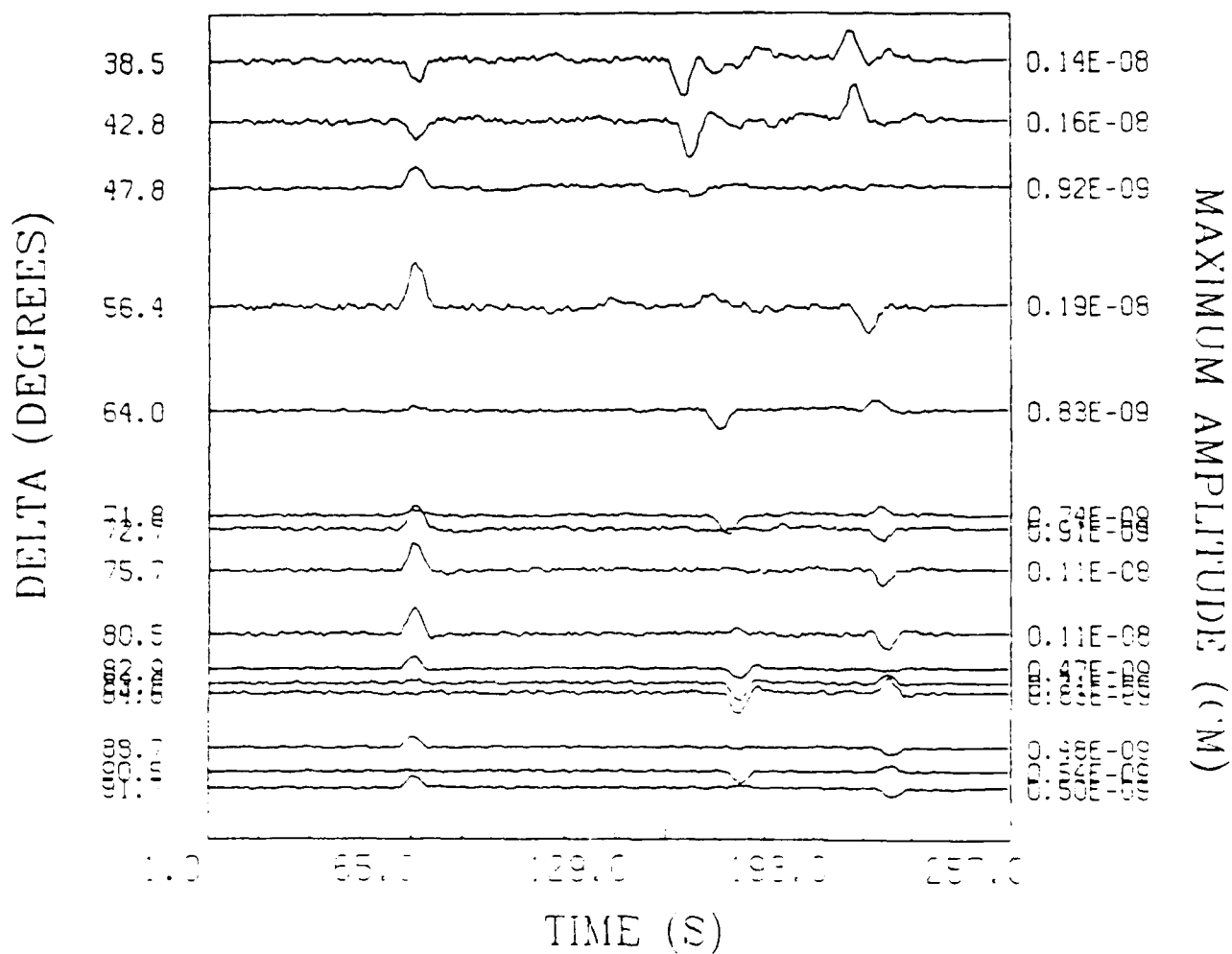
Figure 4. Synthetic seismograms, with 10 % noise, from the source model in Figure 3 and recorded at the stations in Figure 1. The WKBJ method was used to compute the seismograms using the PREM velocity structure.

13

Figure 5. Least squares solution for the moment rate tensor using the noisy seismograms. The source moment rate tensor from Figure 3 has essentially been recovered. The diagonal elements M_{11}, M_{22}, and M_{33} are superimposed on one another.

To use the quadratic programming methods described above it is necessary to first estimate bounds on errors in the data. In this example, absolu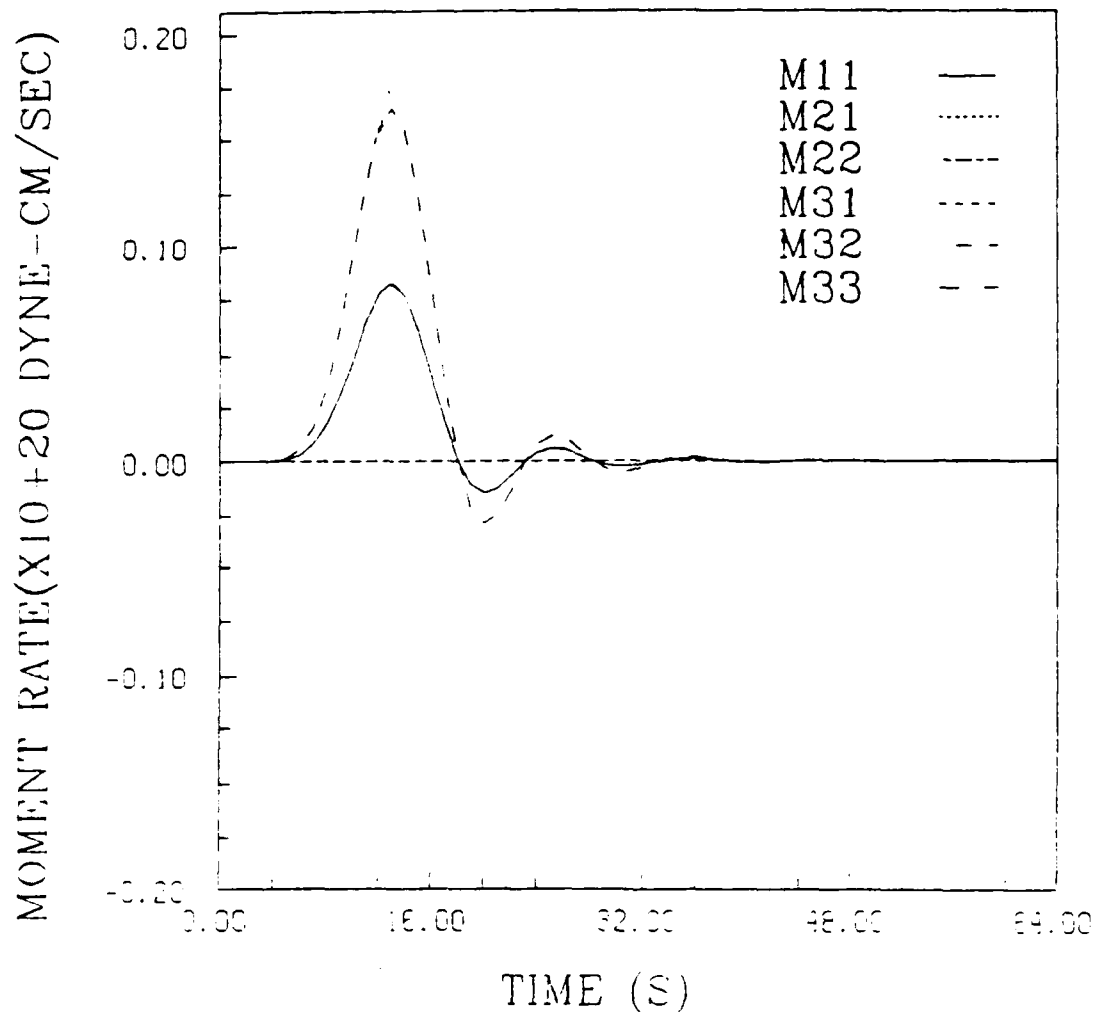te confidence bounds will be used, i.e. constraints (5) will be considered. The bounds were computed by taking the least-squares solution in Figure 5 and predicting the displacement observed at each station. The difference between the vector of observed components, $\mathbf{u}$, and the vector of predicted components, $\mathbf{u_p}$, is used as an estimate of the errors for the data,

$$\epsilon = \mathbf{u} - \mathbf{u_p}$$

In analogy with the 95% confidence interval of normal distributions, twice ϵ was used as confidence intervals on the data. These bounds on the real and imaginary components of the data as a function of frequency are shown in Figure 6 for the third station. Using these estimates of the error bounds it is possible to compute the model with the minimum squared moment tensor trace modulus and the results are shown in Figure 7. Since this is an extreme solution, it exhibits considerably more deviation from the known solution than does the least-squares solution of Figure 5. A similar computation can be performed for the maximum trace modulus, and the moment rate tensor traces for the two extreme models, the maximum and and minimum sum of squared traces, are compared with the least-squares inverse moment rate tensor trace in Figure 8. As expected, the least squares solution lies between the two extreme solutions. What the extreme solutions provide is a measure of the uncertainty in the least-squares solution due to random noise in the data. The effect of increasing the noise in the data is shown in Figure 9. Here, the minimum extreme traces are shown for varying signal to noise ratios. The bounds get progressively wider as the additive noise increases, the lower bound tending toward zero with greater noise. This shows how widening confidence bounds on the data, caused by a decreasing signal to noise ratio, leads to wider bounds on the isotropic moment tensor component.

Lateral heterogeneity in both attenuation and velocity structure also effects moment tensor estimation because it introduces phase and amplitude errors into the data. If the Green function used differs from the real Earth, differences between the observed data and the predicted data will occur. The errors in the Green function enter the above data confidence intervals through the *assumed* data resolution matrix $\mathbf{R_a}$. This is a matrix which relates the observed data to the data predicted assuming a particular velocity structure (Green furction) such as PREM. For an over-determined problem it can be written directly in terms of the assumed Green function $\mathbf{G_a}$ (Aki and Richards 1980, Menke 1984),

$$\mathbf{R_a} = \mathbf{G_a} (\mathbf{G_a^T G_a})^{-1} \mathbf{G_a^T} . \tag{8}$$

Contained in $\mathbf{R_a}$ are the effects of the experimental setup (station distribution, microseismic noise etc.) as well as the effects of lateral heterogeneity. To make this clearer $\mathbf{R_a}$ can be written in terms of the "true" Green function $\mathbf{G_t}$. We make the assumption that the "true"

SPECTRA ERRORS (X10−8 CM)
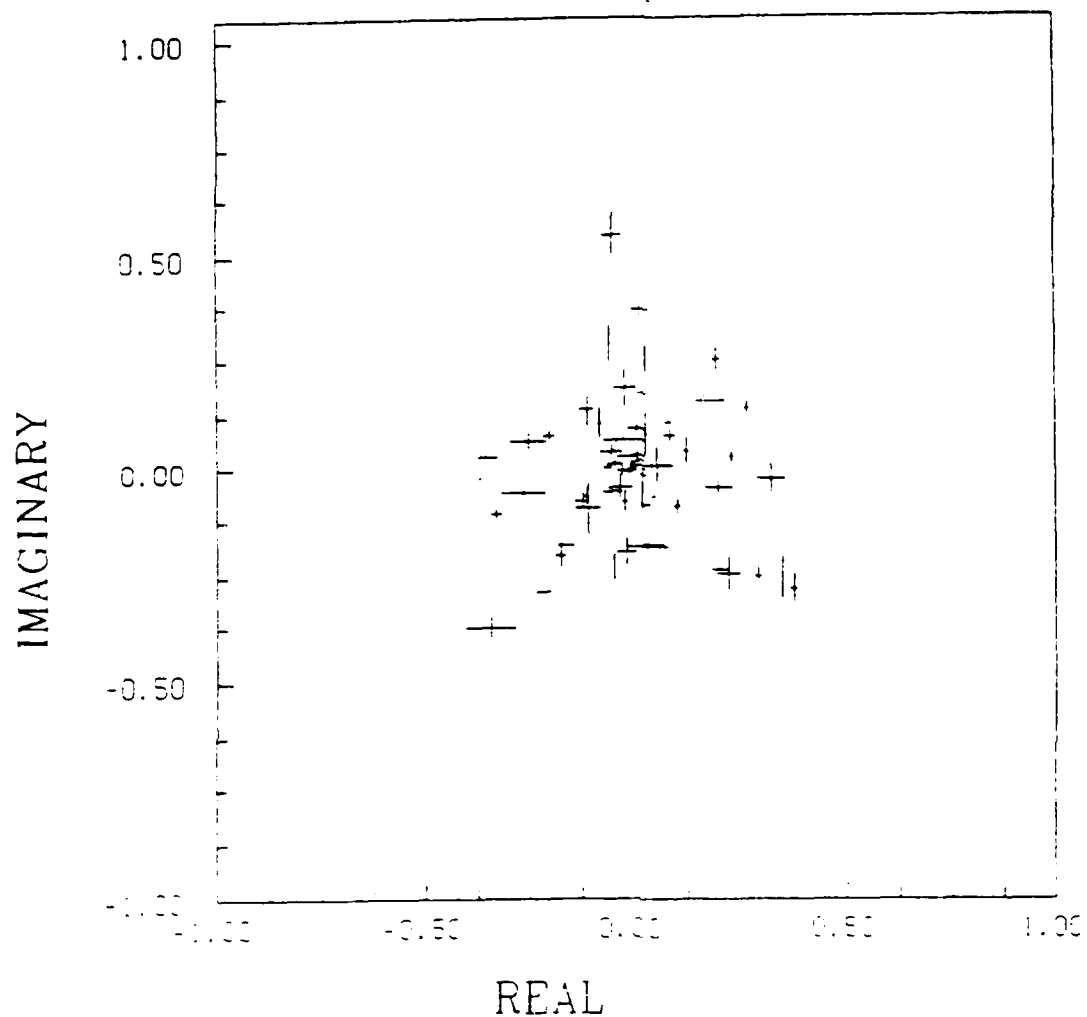
Figure 6. Error bounds on the real and imaginary components of the spectra for the record from station 3. Each point in the figure is at a different frequency.
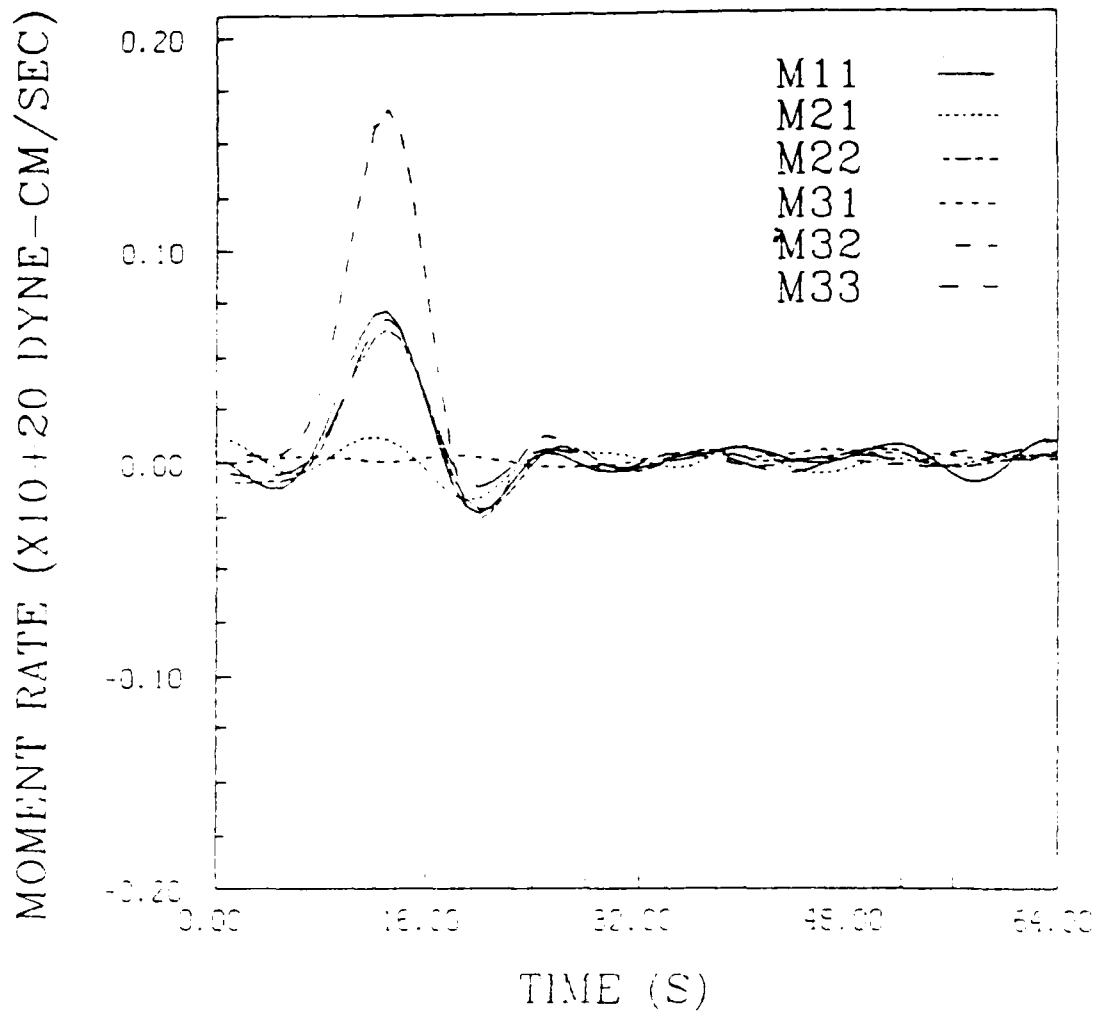
Figure 7. Model having the minimum squared modulus for the moment rate tensor trace. Essential elements of the original source model are recovered but the diagonal elements are no longer identical. Furthermore, the M_{21} and the M_{31} elements are no longer zero.

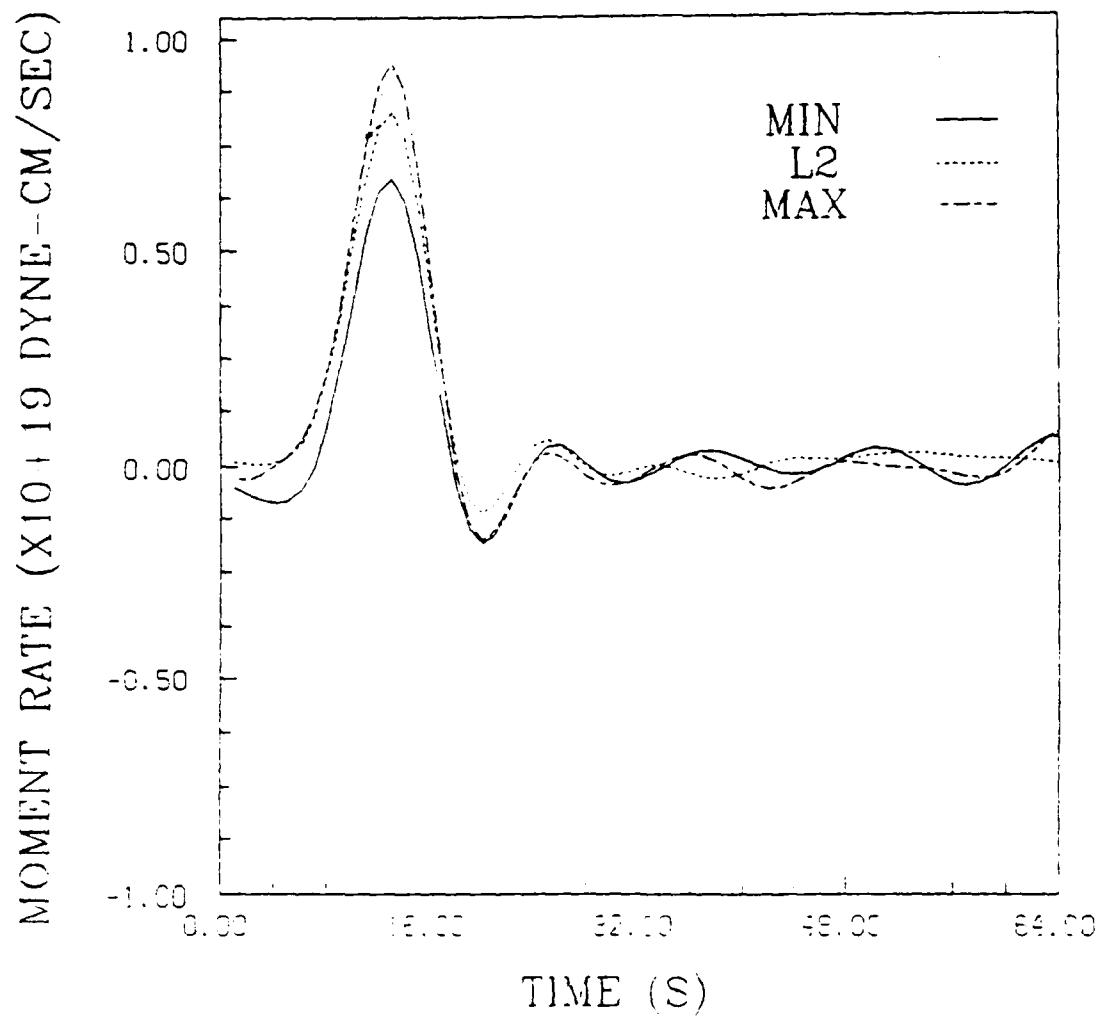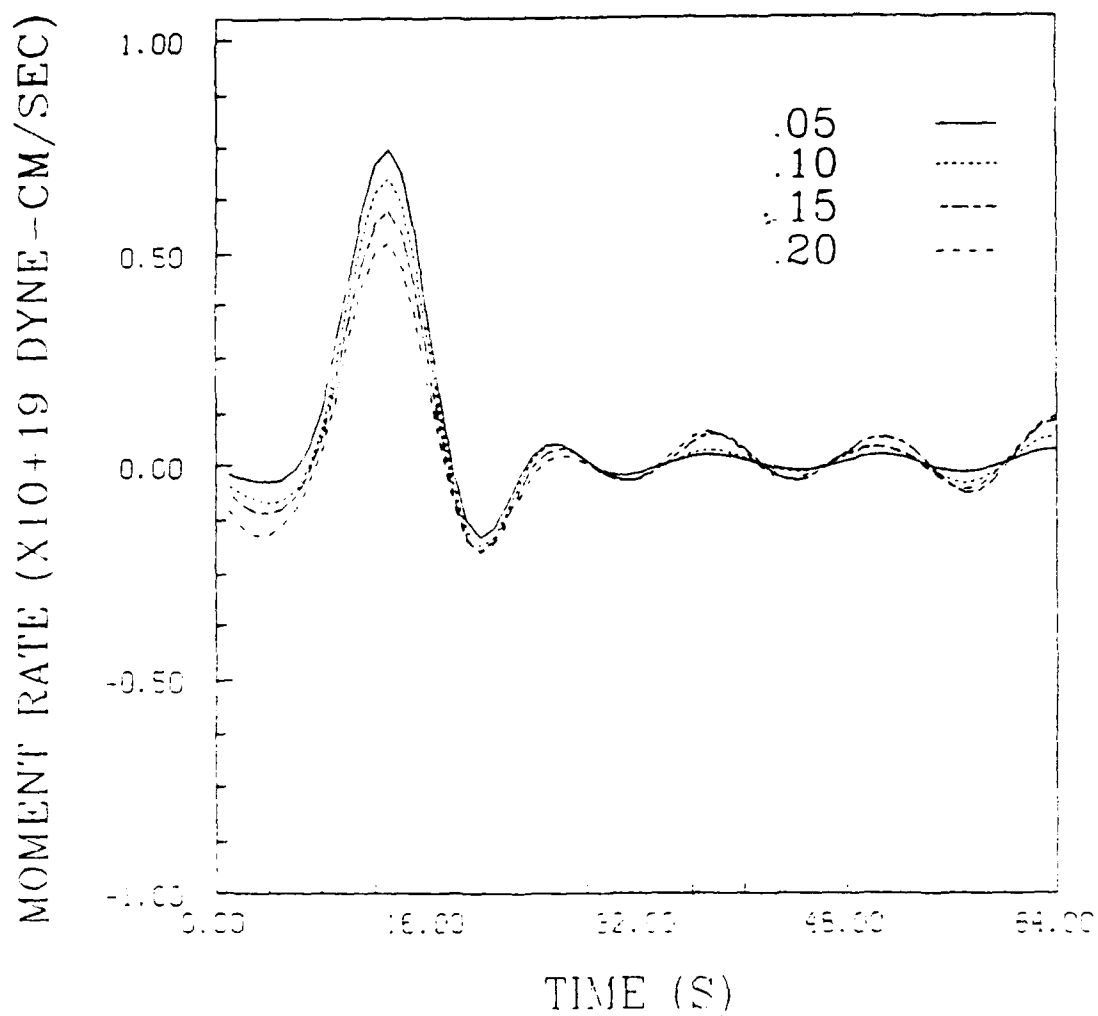**Figure 8.** Comparison of the moment rate tensor traces of the three models: least squares, maximum total squared modulus, minimum total squared modulus.

BONIN MINIMUM TRACES

Figure 9. Effect on the minimum total trace squared solution of varying the signal to noise ratio of the seismograms. It is seen here that as the percentage noise increases the minimum approaches zero.

Green function is a perturbation of the assumed Green function,

$$G_t = G_a + \gamma. \tag{9}$$

We assume that $\|\gamma\| \ll \|G_a\|$, the matrix norm of the Green function perturbation is much less than the matrix norm of assumed Green function. Substituting equation (9) into equation (8) results in the following expression for R_a,

$$R_a = (G_t - \gamma)(G_t^T G_t - G_t^T \gamma - \gamma^T G_t - \gamma^T \gamma)^{-1}(G_t^T - \gamma^T). \tag{10}$$

Neglecting terms higher than first order in γ, factoring out $G_t^T G_t$ and expanding the inverse results in,

$$R_a = G_t (G_t^T G_t)^{-1} G_t^T + G_t (G_t^T G_t)^{-2} G_t^T \gamma G_t^T + G_t (G_t^T G_t)^{-2} \gamma^T G_t G_t^T$$

$$-\gamma(G_t^T G_t)^{-1} G_t^T - G_t (G_t^T G_t)^{-1} \gamma^T$$

The first term on the right is the resolution matrix in terms of the "true" Earth model and Green function, G_t. Therefore, the confidence bounds, ϵ in equation (5) are given by,

$$\epsilon = (I - R_t - G_t (G_t^T G_t)^{-2} G_t^T \gamma G_t^T - G_t (G_t^T G_t)^{-2} \gamma^T G_t G_t^T \tag{11}$$

$$+\gamma(G_t^T G_t)^{-1} G_t^T + G_t (G_t^T G_t)^{-1} \gamma^T)u.$$

R_t does not depend on the perturbations of the Green function, only on the structure of the experiment. It is now clear that, even if the experiment were structured such that the data were perfectly resolved, the presence of lateral heterogeneity, nonzero γ, could still produce non-zero confidence bounds on the data. Therefore, if the differences between the observed and predicted data are used as confidence bounds on the data, then the effect of model errors will be incorporated in the extreme model estimates. In the presence of lateral heterogeneity the extreme bounds on the model properties will be wider.

A synthetic test was also performed to explore the effect of the lateral heterogeneity. The test was similar to the previous one with the earthquake at 625 km depth and the station distribution as shown in Figure 1. The mechanism is the same as before (Figure 3) but now the earth model is not homogeneous. Instead, each path consists of a perturbed version of PREM. Specifically, a 2% random perturbation in velocity was added at each depth in the model with independent perturbations for each ray path. The lateral heterogeneity results in the synthetic seismograms shown in Figure 10 with errors in the phase and amplitude present. When the extremal solutions, minimum and maximum trace squared, are computed and presented with the least-squares solution, they differ substantially (Figure 11). By comparing these models with similar models derived with 10% random noise present (Figure 8) it is seen that the effect of lateral heterogeneity can be quite strong.

20
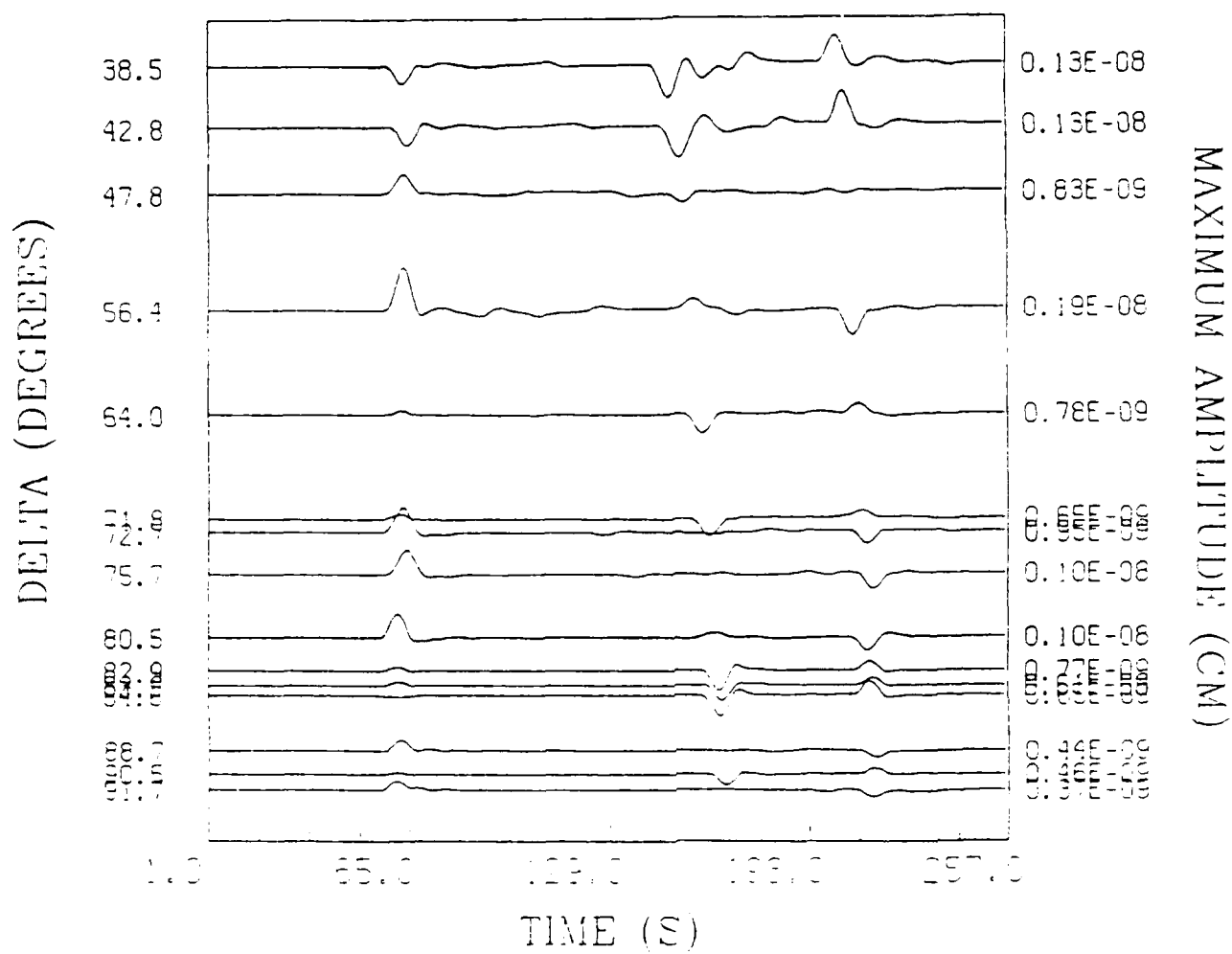
Figure 10. Seismograms with perturbed arrivals due to lateral velocity inhomogeneities. Two percent random perturbations on the PREM model were applied to each source-receiver path
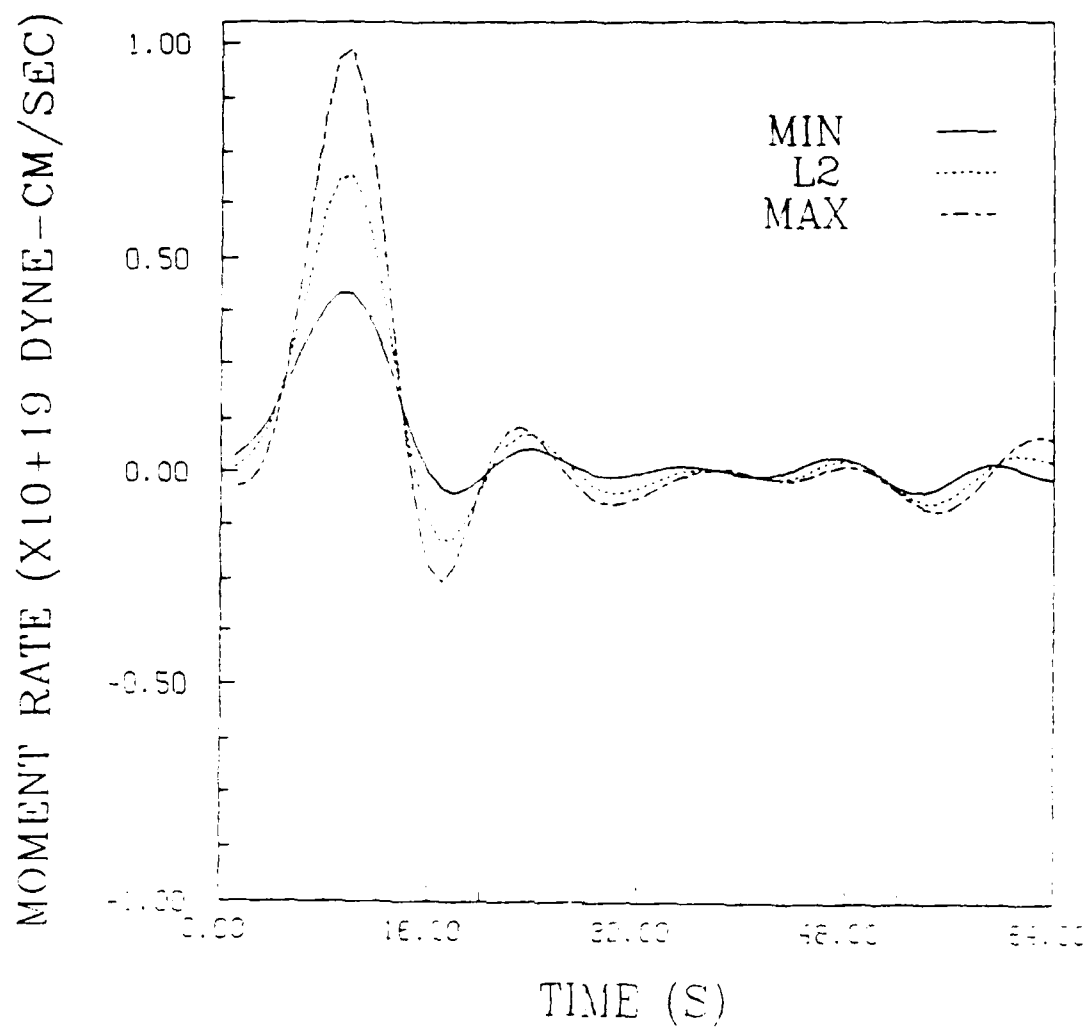
21

Figure 11. Moment rate tensor traces of the least squares and maximum and minimum extreme trace solutions. These solutions are the result of inverting the perturbed seismograms in Figure 10 while assuming a laterally homogeneous velocity structure (PREM).

These examples demonstrate some strengths and weaknesses of the approach taken so far. First, the error bounds derived depend directly on the knowledge of the velocity structure, the point source assumption, and the microseismic noise. This dependence is through the least squares solution which is used to construct the predicted data. For an over-determined problem, as our knowledge improves, for example through the modeling of lateral heterogeneities, the bounds on the data will narrow. However, with the absolute bounds used, the strict inequalities of equation (5), can be either too restrictive or too wide. This is because the confidence bounds must be satisfied exactly, no single point may exceed the bounds. Therefore, the bounds must be made wide in order for the probability that any data exceeds these bounds to be small (Oldenburg 1983). This can be improved by the use the statistical bounds given in equation (6).

Results for the Bonin Islands earthquake

Given the results of these synthetic tests which illustrate the effects of random noise and Earth heterogeneity, we can now return to the inversion of the data shown in Figure 2 for the Bonin Islands earthquake. Recall that the basic question to be answered is whether the source of this earthquake had a significant isotropic component. As a prelude to the inversion of the actual data, one further set of synthetic tests was performed. Using the station distribution and event location identical to the Bonin Islands earthquake and assuming 10% random noise and 2% lateral velocity perturbations, the mimimum trace squared solution was obtained for a series of sources having different relative sizes of the isotropic component. We consider an isotropic component to be identifiable if it is distinguishable from other features of the solution which are caused by the mapping of microseismic noise and Green function errors into the solution. The results, which are shown in Figure 12, allow one to ask the question: What proportion of isotropic component must be present in the source in order for it to be unambiguously identified in the inversion results? The answer is fairly high: more than 10% of the source has to be due to volume change alone. When the same exercise was conducted using perturbations of 5% at least 20% of the source had to be isotropic for detection. Thus it may not be possible to discern a small isotropic moment tensor without more and better data and without better modelling of the velocity structure.

Turning now to the data shown in Figure 2, the least squares solution is shown in Figure 13. The main part of the source is an initial pulse of about 20 sec duration, which reflects the bandwidth of the instrumentation. For this initial pulse, the principal axes of the deviatoric part of the source have the approximate orientations (plunge, azimuth): tension axis = (10, 42); intermediate axis = (45, 144); compression axis = (40, 320). This is similar to the Harvard solution (Bull. ISC): tension axis = (16, 49); intermediate axis = (23, 146); compression axis = (61, 287). It is also generally consistent with the fault plane solutions of other earthquakes in this region (Burbach and Frolich, 1986). However, the primary interest in this study is the trace of the moment tensor and it is obvious that

23
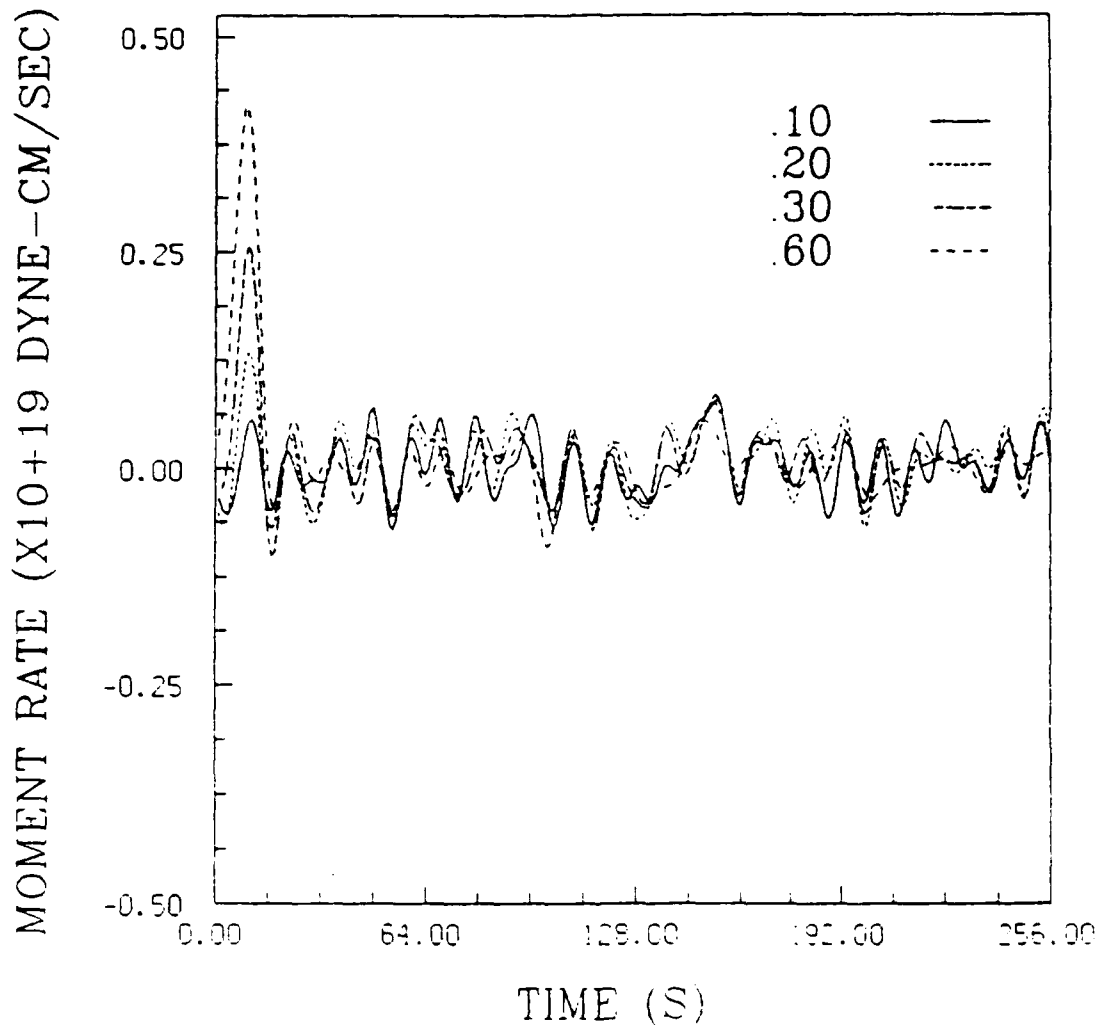
Figure 12. Simulation of the moment rate traces in the minimum total trace squared solution for varying proportions of the isotropic component. The velocity structure was again assumed to be PREM while the structure used to generate the seismograms contained two percent perturbations of PREM. The proportion of isotropic component is given by the ratio of the isotropic component to the sum of the absolute values of the moment components.

24

BONIN ISLANDS L2 SOLUTION
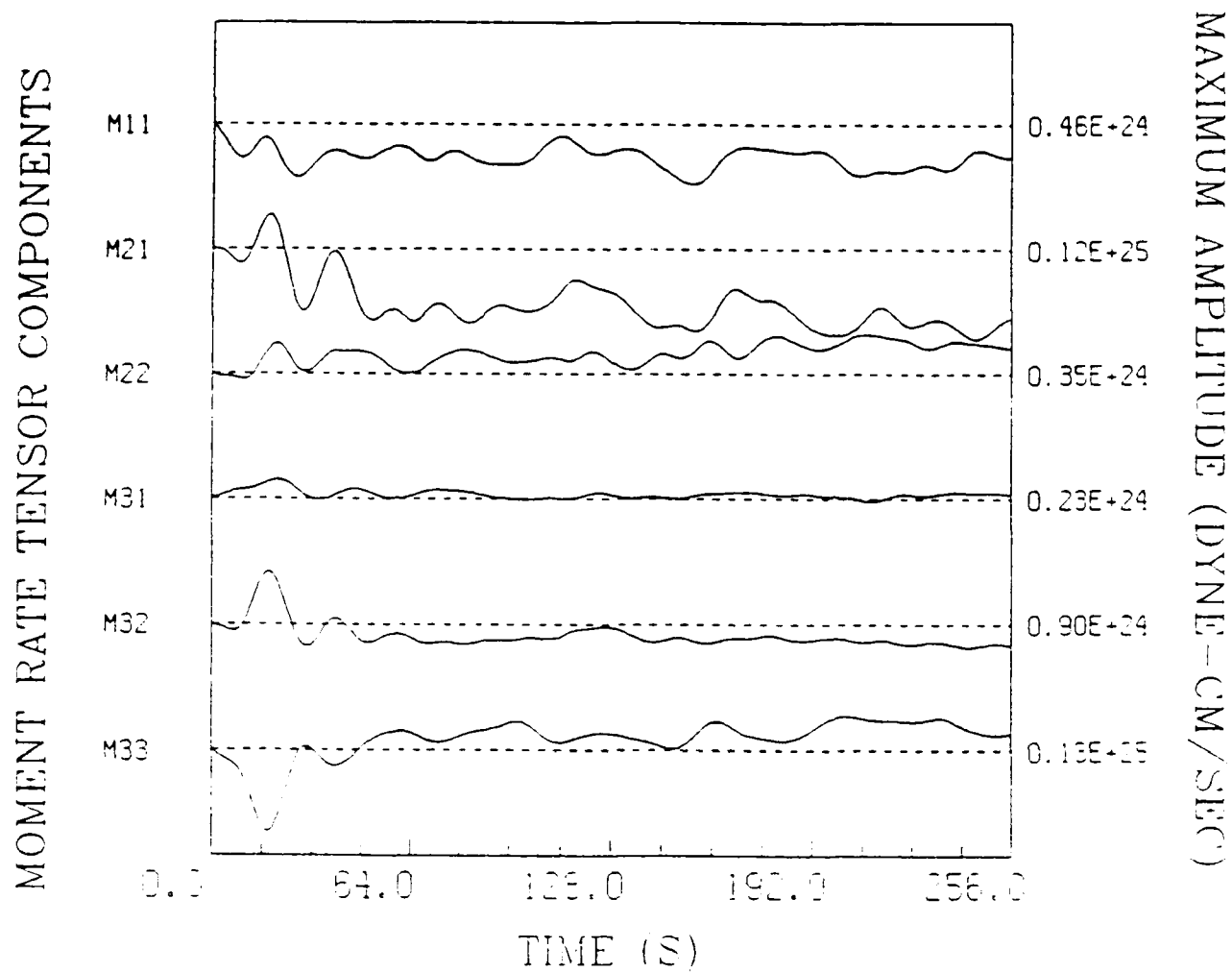
Figure 13. The least squares moment rate trace solution for the Bonin Islands event. This is the result of inverting the seismograms in Figure 2 assuming a PREM earth.

BONIN ISLANDS MODELS
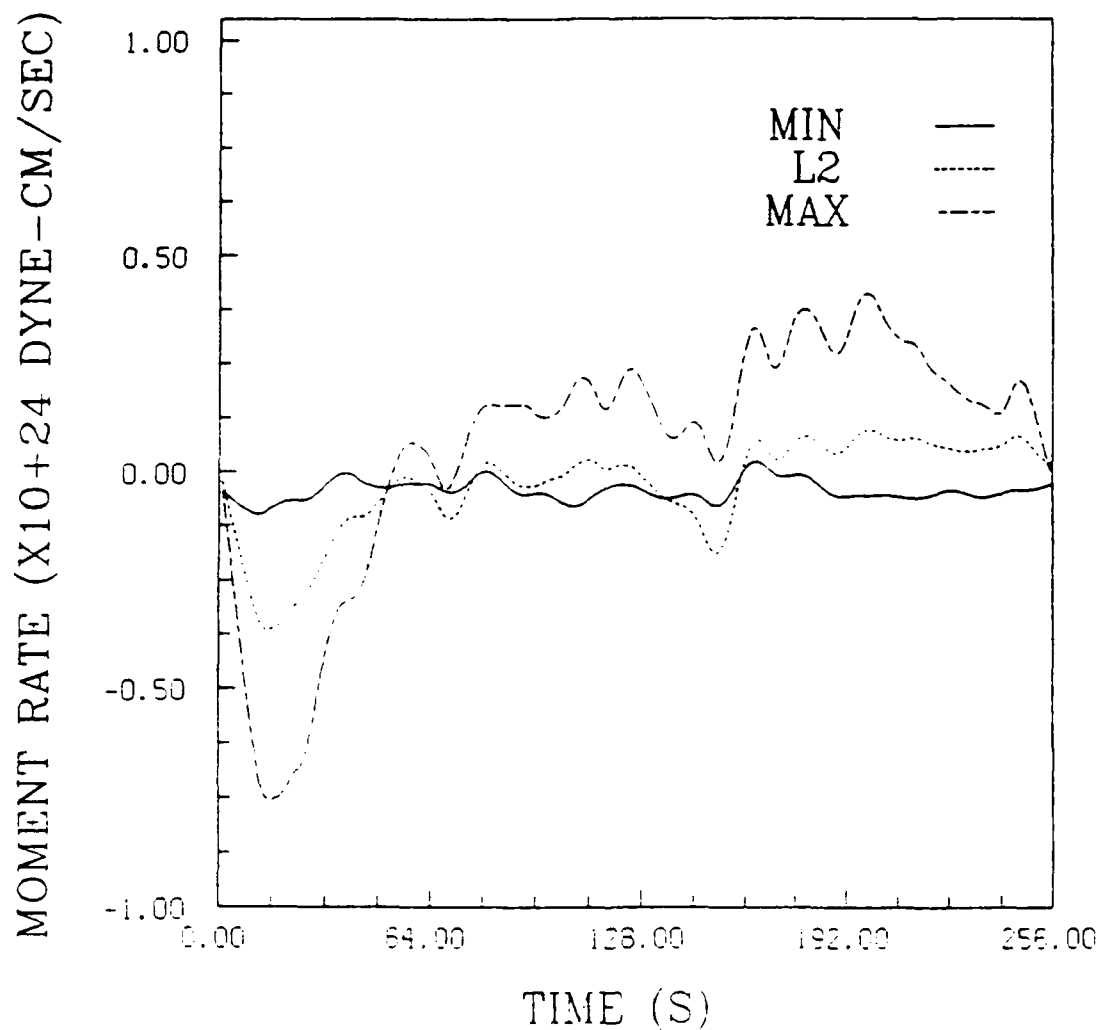
Figure 14. Comparison of the traces for the three models: least squares, maximium moment rate trace squared, and minimum moment rate trace squared. The minimum trace is essentially zero but the wide range in the solutions suggests that the isotropic component is not well constrained.

this is significantly different from zero for the least-squares solution, because in Figure 13 the M_{33} component is much larger than the M_{11} and M_{22} components. This trace from the least-sqaures solution is shown in Figure 14 along with maximum and minimum trace solutions obtained with the quadratic programming approach. The error bound assumed in the extremal solutions was twice the root-mean-square error of the least-squares solution. The least-squares solution has a prominent negative isotropic component in the first 20 sec which could be interpreted as a volume change at the source. Unfortunately, the mimimum extreme solution shows that, given the uncertainty in the data and the Green functions used in the inversion, this volume change suggested by the least-squares solution may not be significant. On the basis of the synthetic tests and the fairly large signal to noise ratio in the data (Figure 2), it seems likely that lateral heterogeneity is largely responsible for the width of the bounds and therefore the weakness of any conclusion which may be drawn from these results.

In order to test if the minimum volume change is significantly different from zero, the best fitting solution with the trace constrained to be zero could be found. Then a Monte Carlo simulation, considering all error sources, could be used to compile a population of waveform data sets. An inversion of these data sets would give statistics on the zero trace solutions. This would allow one to statistically test if the minimum squared trace solution is significantly different from zero. We feel that, at present, models of velocity and attenuation lateral heterogeneity are not yet adaquate for this. Instead, we rely on a comparison of the isotropic component with the other moment tensor components to estimate significance.

Nuclear Explosion Sources

One seismic source which is known to have a large isotropic component is a nuclear explosion. It is an ideal case for the computation of extremal moment tensor models. Near source data from a nuclear explosion can be used to compute upper and lower bounds on squared moment tensor trace, which is a measure of the volume change associated with the source. Thus the solutions are, respectively, the most and least explosion-like solutions. This has important applications in the verification of nuclear explosions because these solutions provide best and worst cases by which to decide if an event was a nuclear explosion.

The Harzer experiment of June 6, 1981, a nuclear explosion of equivalent magnitude 5.5 at a depth of 637 m was recorded by eight, three component, broadband, digital, accelerometers. The details of the collection and interpretation of the data can be found in Johnson (1988) and will only be briefly reviewed here. The near source network was azimuthally distributed around the epicenter with stations from 2.4 km to 6.6 km from the event (Figure 15). The velocity records are shown in Figure 16. The network was located in the Silent Canyon Caldera, a heterogeneous velocity structure. The averaged one-dimensional velocity structure in this Caldera has been studied by Leonard and Johnson (1987) and their model was used in moment tensor inversions. A modified reflectivity method (Kind 1978) was
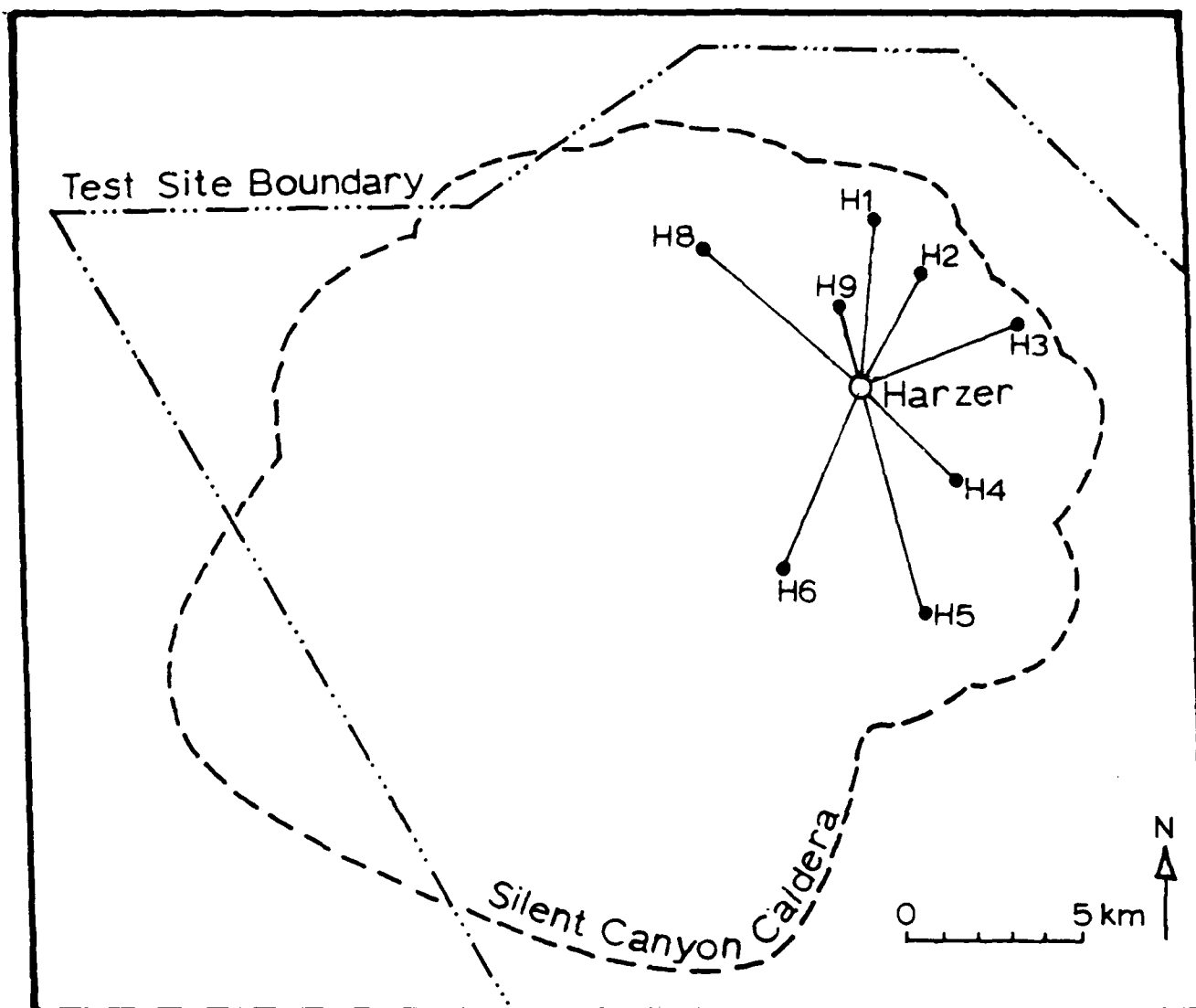
Figure 15. Harzer experimental setup. Station distribution within the Silent Canyon Caldera. The stations were three component broadband accelerometers.
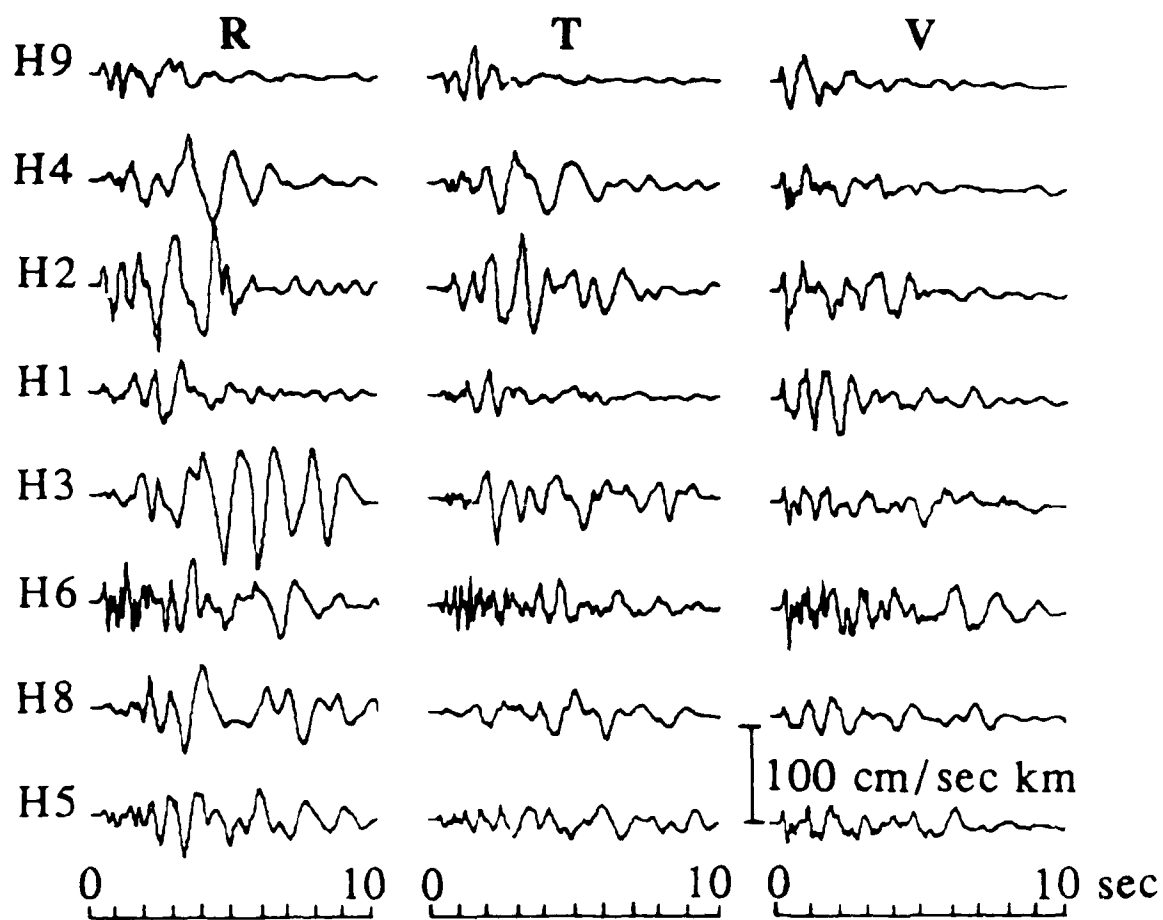
28

Figure 16. Rotated velocity records from the Harzer explosion. Note the significant energy on the transverse components.

used to compute the Green functions.

Because of difficulties at one of the sites, seven stations were used in the inversion, giving a total of 21 components. The least-squares solution for the moment rate tensor of this overdetermined problem is shown in Figure 17. The most important part of the moment rate tensor is the initial short-period pulse which is followed by longer-period oscillations which are less coherent and more poorly resolved. This initial pulse is most pronounced on the trace components M_{11}, M_{22}, and M_{33}, although there is still energy on the off-diagonal elements, such as M_{23}. The M_{11} and M_{22} elements are fairly similar in their time dependence, but the M_{33} element is somewhat different, containing a large secondary pulse at about 2 seconds. When this solution is combined with the Green functions, predicted seismograms are obtained which do a reasonably good job of explaining the major features of the observed data in Figure 16, with average correlation coefficients of about 0.5. However, there still remain significant differences between the predicted and observed seismograms, particularly on the transverse components. Much of this difference can probably be attributed to effects which were not taken into account in the modelling, such as lateral heterogeneities and scattering in the wave propagation and secondary source effects such as spall.

Given that the source has been less than perfectly resolved by the least-squares solution for the moment tensor, what can be said about the uncertainty in the explosive part of the source? This question is answered in Figure 18 which shows the least-squares solution for the moment rate tensor trace along with the estimates for the minimum and maximum moment rate tensor traces. It is clear that an initial compressional pulse is present on all three solutions. Thus, even in the presence of fairly large error bounds due to both random noise and deficiencies in the modelling process, it can be concluded that this source has a clear explosive component. The extremal solutions are also useful in associating an uncertainty with the first pulse on the trace, which is directly related to the yield of the explosion.

Up to this point all of the calculations have employed the local error bounds of equation (5), but there are situations where the global error bounds of equation (6) might be preferred. The results of using these two types of error bounds are compared in Figure 19 for the minimum trace solution. In this particular case the choice of bound does not cause enough difference in the results to affect any of the conclusions based upon them.

Conclusions

A method has been developed by which extreme models of the time-varying moment tensor may be constructed. The method has the potential to answer many interesting geophysical questions. In particular, it is now possible to assess the presence or absence of volume change (isotropic component) in seismic sources. It has been comonly assumed that the isotropic component of the moment tensor vanishes. We believe that this assumption has not been adaquately examined and that this method can be used for this purpose.

30

HARZER L2 SOLUTION
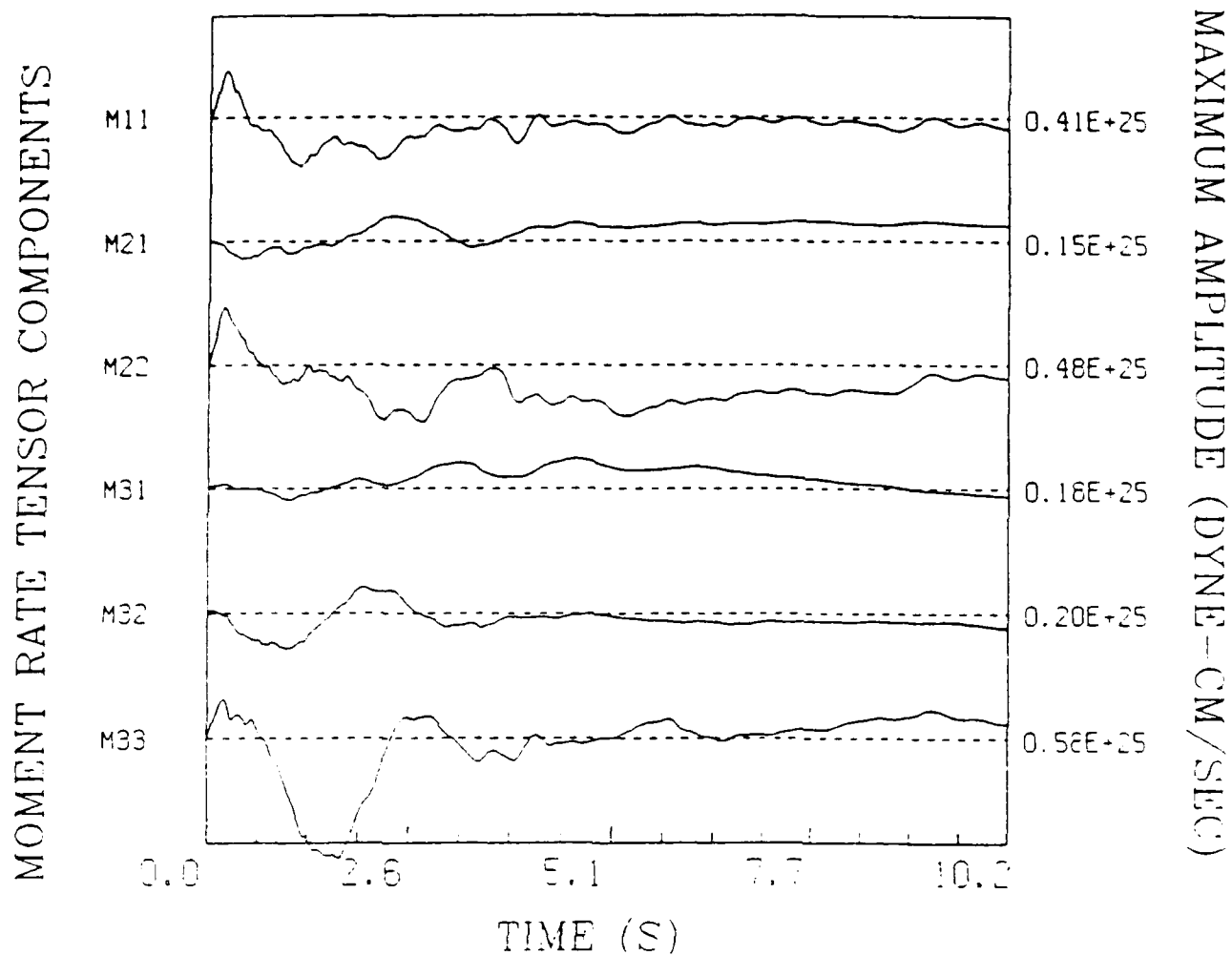
Figure 17. Least squares solution for the Harzer explosion's moment rate tensor.

31
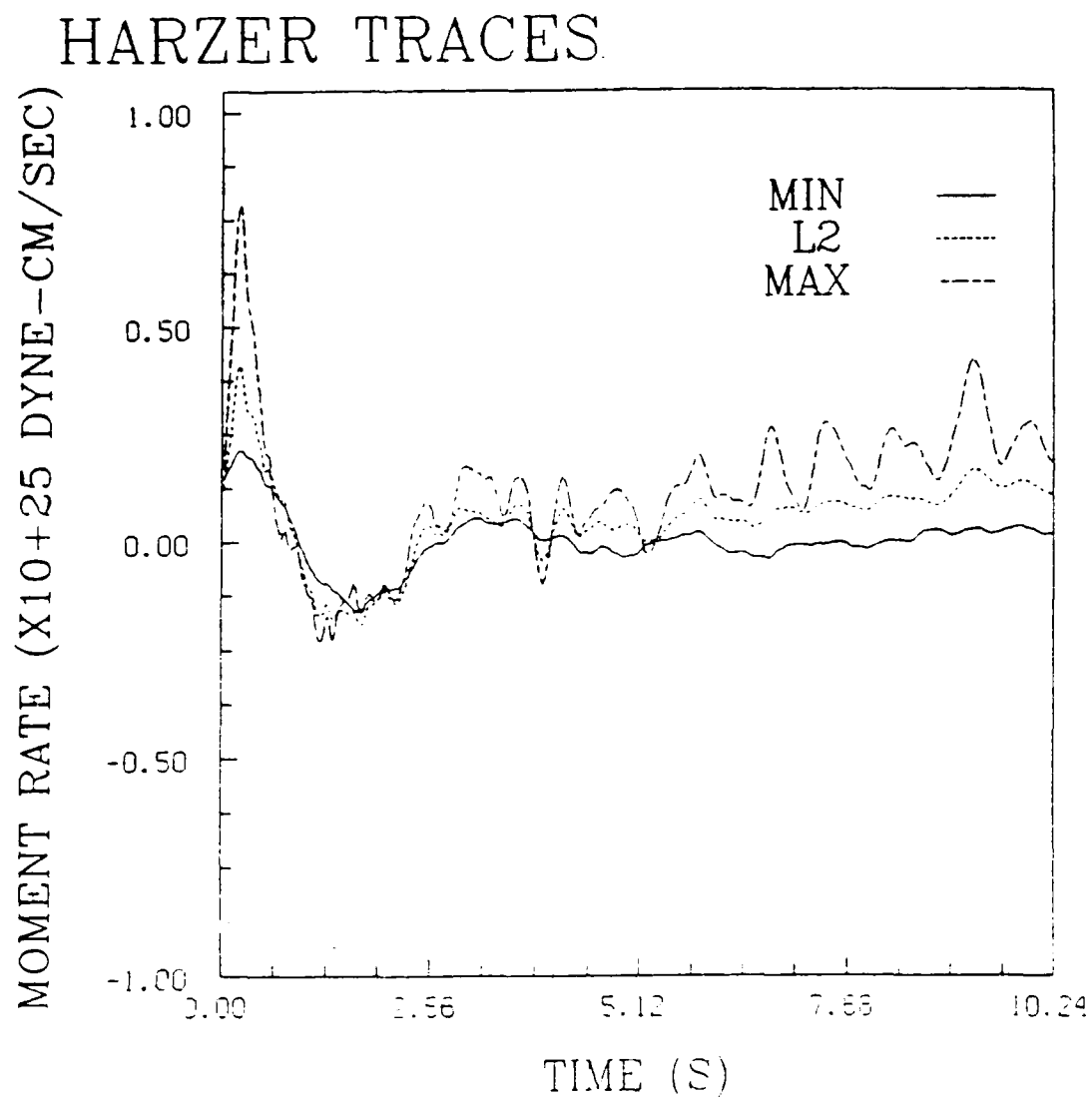
HARZER TRACES

Figure 18. Moment rate traces for the least squares, maximum and minimum trace squared solutions. There is a wide range in the models for the early pulse but a definite isotropic component is present in all models.

HARZER MINIMUM BOUNDS
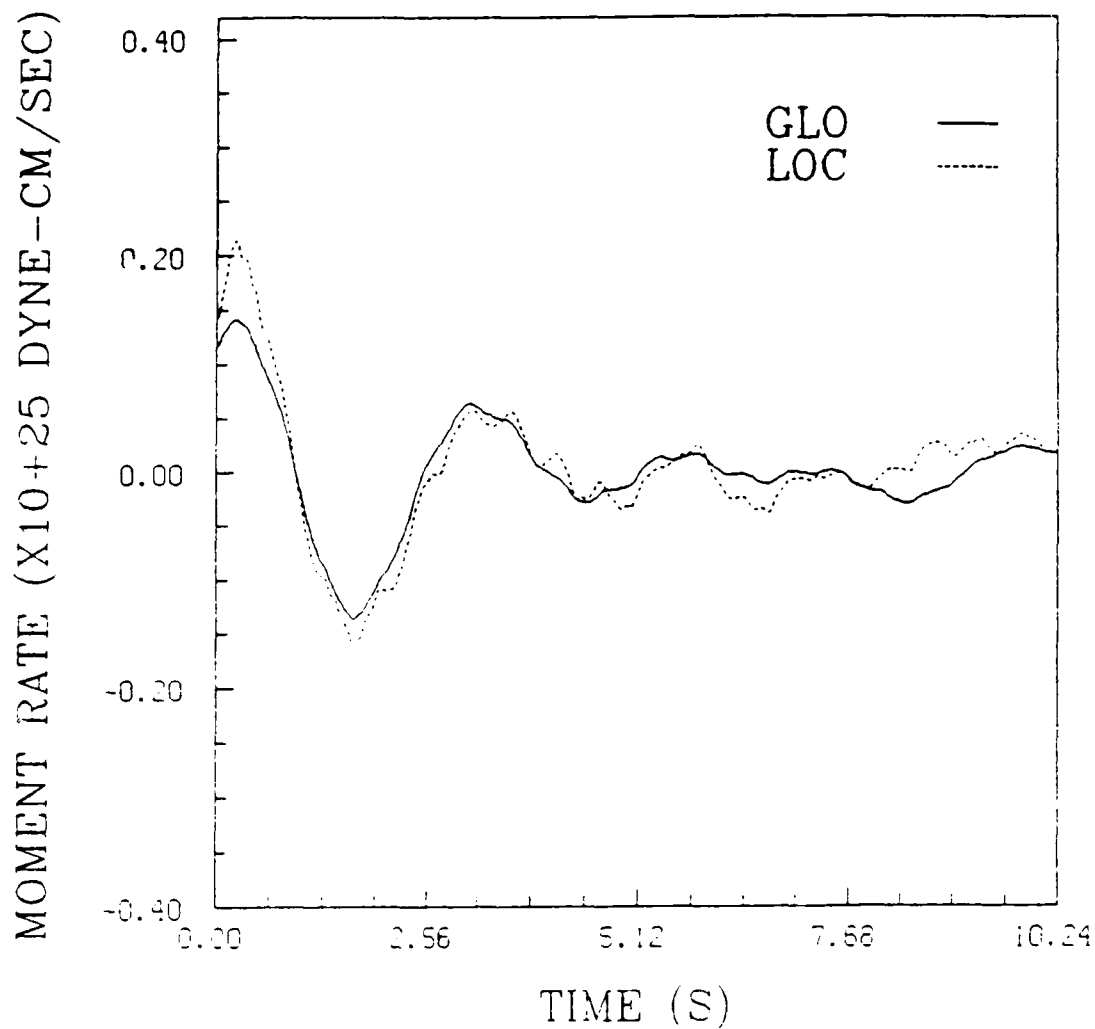
Figure 19. Minimum moment rate trace squared solutions computed using the strict data bounds of equation (5) and the global data bounds of equation (6). Again, both models have an obvious isotropic component.

The two applications described above illustrate two areas in which extreme bounds on the isotropic component are useful: deep earthquakes and nuclear explosions. Surely, many others are possible. One exciting aspect of the technique is that it makes full use of the waveforms. With the advent of new networks of wide dynamic range, broad band digital seismometers such as GEOSCOPE and IRIS greater resolution will be possible. As can be seen from the Harzer inversions, even high frequency data can give exellent inversion results.

The method described in this paper provides an extreme estimate of some aspect of the moment tensor, given the recorded seismograms and an estimate of their uncertainty in either the time domain or frequency domain. This uncertainty should include all possible sources of error, including random noise, the source location, the earth model used in calculating the Green functions, and the method used to calculate the Green functions. In some situations it may be possible to make *a priori* estimates of all these errors, but in general this will not be possible. In this paper we have proposed the alternative procedure of using the residual of the least-squares solution as an estimate of the total error. While this procedure has the undesireable feature that the error estimate depends upon the data, it does provide a procedure that can be used in all instances and it seems to have given reasonable results in the two cases considered. The method is flexible in the sense that the error constraints can be applied in either a local or global sense.

Acknowledgments

34

References

Backus, G. E., M. Mulcahy, 1976. Moment tensors and other phenomenological descriptions of seismic sources - I. Continuous displacement, Geophys. J. R. Astr. Soc., 46, 341-361.

Bracewell, R. N. 1978. The Fourier Transform and Its Application. McGraw-Hill, Inc. New York, New York.

Bulletin of the International Seismological Centre, 1985, 22, no. 10, 27-29.

Burbach, G. V., C. Frolich, 1986. Intermedi 'e and deep seismicity and lateral structure of subducted lithosphere in the circum-Pacific region, Rev. Geophys., 24, 833-874, 1986.

Chapman, C. H., 1978. A new method for computing synthetic seismograms, Geophys. J. R. Astr. Soc., 54, 481-518.

Dantzig, G. B. 1963. Linear Programming and Extensions, Princeton University Press, Princeton, New Jersey.

Dziewonski, A. M., D. L. Anderson, 1981. Preliminary reference Earth model, Phys. Earth Planet. Inter., 25, 297-356.

Dziewonski, A. M., Chou, T.-A., Woodhouse, J. H. 1981. Determination of earthquake source parameters from waveform data for studies of global and regional seismicity, J. of Geophys. Res., 86, 2825-2852.

Dziewonski, A. M., Gilbert, F. 1974. Temporal variation of the seismic moment and the evidence of precursive compression for two deep earthquakes, Nature, 247, 185-188.

Fitch, T. J., McGowan, D. W., Shields, M. W., 1980. Estimation of the seismic moment tensor from teleseismic body wave data with applications to intraplate and mantle earthquakes, J. of Geophys. Res., 85, 3817-3828.

Gilbert, F., Buland, R. 1976. An enhanced deconvolution procedure for retrieving the seismic moment tensor from a sparse network, Geophys. J. R. Astron. Soc., 50 251-255.

Gilbert, F., Dziewonski, A. M. 1975. An application of normal mode theory to the retrieval of structural parameters and source mechanisms from seismic spectra, Philos. Trans. R. Soc. London, Ser. A, 278, 187-269.

Hodder, A. P. W. 1984. Thermodynamic constraints on phase changes as earthquake source mechanisms in subduction zones, Phys. of Earth and Planet. Inter., 34, 221-225.

Johnson, L. R., 1988. Source characteristics of two underground nuclear explosions, in press, Geophys. J. R. Astr. Soc.

Julian, B. R. 1986. Analyzing seismic-source mechanisms by linear-programming methods, Geophys. J. R. astr. Soc., 84, 431-443.

Kanamori, H and J. W. Given 1981. Use of long-period surface waves for rapid determination of earthquake-source parameters, Phys. Earth planet. Int., 37, 8-31.

Kirby, S. H., 1987. Localized polymorphic phase transformations in high-pressure faults and applications to the physical mechanism of deep earthquakes, J. Geophys. Res., 92, 13789-13800.

35

Kind, R., 1978. The reflectivity method for a buried source, J. Geophys., 44, 603-612.

Leonard, M. A. and L. R. Johnson 1987. Velocity structure of Silent Canyon Caldera, Nevada Test Site, Bull. Seis. Soc. of Amer., 77, 597-613.

McCowan, D. W. 1976. Moment tensor representation of surface wave sources, Geophys. J. R. astr. Soc., 44, 595-599.

Meade, C., Jeanloz, R., 1988. Ultra-high pressure fracturing: First experimental observations of deep focus earthquakes, EOS, 69, 490.

Menke, W. 1984. Geophysical Data Analysis: Discrete Inverse Theory, Academic Press, Orlando, Florida.

Okal E. A. and R. J. Geller 1979. On the observability of isotropic seismic sources: the July 31, 1970 Colombian earthquake, Phys. Earth Planet. Inter., 18, 176-196.

Oldenburg, D. W. 1983. Funnel Functions in Linear and Nonlinear Appraisal, J. Geophys. Res., 88, 7387-7398.

Parker, R. L. and M. K. McNutt 1980. Statistics for the one-norm misfit measure, J. of Geophys. Res., 85, 4429-4430.

Riedesel, M. A. and T. H. Jordan 1985. Detectability of Isotropic Mechanisms for deep-focus earthquakes, Eos, 66, 46, 1086.

Silver, P. G. and T. H. Jordan 1982. Observations of low-frequency moment spectra of several large seismic events, Eos, 63, 18, 373.

Sipkin, S. A. 1982. Estimation of earthquake source parameters by the inversion of waveform data: Synthetic waveforms, Phys. Earth Planet. Inter., 30, 242-259.

Sipkin, S. A. 1986. Interpretation of non-double-couple earthquake mechanisms derived from moment tensor inversion, J. of Geophys. Res., 91, 531-547.

Stump, B. W. and L. R. Johnson 1977. The determination of source properties by the linear inversion of seismograms, Bull. Seis. Soc. Am., 67, 1489-1502.

Tanimoto, T. and H. Kanamori 1986. Linear Programming approach to moment tensor inversion of earthquake sources and some tests on the three-dimensional structure of the upper mantle, Geophys. J. R. astr. Soc., 84, 413-430.

Second Order Moment Tensors of Microearthquakes at The Geysers Geothermal Field, California

Daniel R. H. O'Connell

Department of Geology and Mineralogy, The Ohio State University,
Columbus, Ohio 43210

Lane R. Johnson

Center for Computational Seismology, Lawrence Berkeley Laboratory,
Department of Geology and Geophysics, University of California,
Berkeley, California 94720

ABSTRACT

The Geysers geothermal field is the site of intense microseismicity which appears to be associated with steam production. It appears that focal mechanisms of earthquakes at The Geysers vary systematically with depth, but P-wave first-motion focal mechanism studies have been hampered by inadequate resolution. In this study an unconstrained frequency domain moment tensor inversion method is used to overcome P-wave first-motion focal sphere distribution problems and to investigate microearthquake source properties . A goal was to investigate the feasibility of using waveforms to invert for the second-order moment tensor of microearthquakes in the complex setting of The Geysers. Derived frequency-domain moment tensors for two earthquakes were verified by mechanisms estimated from P-wave first motions and required far fewer stations. For one event, 19 P-wave first motions were insufficient to distinguish between normal-slip and strike-slip focal mechanisms, but a well constrained strike-slip solution was obtained from the waveform principal moment inversion using data from 6 stations. Improved waveform focal mechanism resolution was a direct consequence of using P and S-wave data together in a progressive velocity-hypocenter inversion to minimize Green function errors. The effects of hypocenter mislocation and velocity model Green function errors on moment tensor estimates were investigated. Synthetic tests indicate that these errors can introduce spurious iso-

37

tropic and CLVD components as large as 26% for these events whereas principal moment orientations errors were <8°. In spite of unfavorable recording geometries and large (0.6 km) station elevation differences, the results indicate that waveform moment tensor estimates for microearthquake sources can be robust and constrain source mechanisms using data from a relatively small number of stations.

1. Introduction

Estimates of seismic source properties are among the most important pieces of information extracted from recordings of microearthquakes. Source studies using microearthquakes can constrain the mechanism and geometry of faulting and provide estimates of principal stress orientations. These estimates form a basis for interpreting deformation associated with the earthquakes and possible relations between seismicity and tectonic stresses.

The Geysers is the world's largest generator of electricity using geothermal energy and the site of intense microseismicity. The rate of seismicity at The Geysers is 45 times the regional rate (Ludwin et al., 1982). Most earthquakes occur within or just below the shallow steam production zone at depths of 2 to 4 km below the mean surface elevation. At The Geysers the relationship between seismicity, tectonic, and locally induced stresses is unclear. Although it appears that seismicity at The Geysers is induced by steam production activities, a specific mechanism has not been determined (Oppenheimer, 1986; Eberhart- Phillips and Oppenheimer, 1984; Bufe et al., 1981). Bufe et al. (1981) suggested that the wide range in fault plane solutions found at The Geysers were a function of time.

Oppenheimer (1986) estimated the stress field orientation at The Geysers from 210 fault plane solutions. Based on agreement of the extensional principal stress direction estimated from the seismicity as a whole with that obtained from regional geodetic data (Prescott and Yu, 1986), he concluded that regional tectonic stresses are much larger than the stresses induced locally through geothermal activities. Oppenheimer (1986) found that shallow earthquake focal mechanisms are dominantly strike-slip and reverse whereas deeper focal mechanisms predominantly exhibit normal faulting. He concluded that focal mechanisms at The Geysers are a function of depth. His estimation of stress-field orientation and

38

variation of focal mechanisms with depth were hampered by the common problem of nonunique fault plane solutions.

For many shallow events there is an ambiguity between pure strike-slip and pure dip-slip mechanisms. These ambiguities are not due to a paucity of P-wave first motion data. Numerous P-wave first motions are available for earthquake at The Geysers because an extensive seismic recording network has been operated since 1976 in The Geysers area by the U.S. Geological Survey (USGS). Often however, P-wave first motions are absent from the central portions of the upper focal hemisphere for shallow events because no stations are close enough to the epicenter. This problem persists despite an average station spacing of about 2 km in the source area and can be attributed primarily to two factors. The earthquakes are very shallow, generally 2 to 4 km below mean station elevations, and velocity gradients (Figure (1)) are large. These two factors combine to severely reduce the number of observations in the central portion of the upper focal hemisphere. Observations from distant stations that sample the central portion of the lower focal hemisphere are absent due to attenuation of microearthquake signals. Oppenheimer (1986) noted that for some events, fault plane solutions were completely ambiguous; strike-slip, reverse-slip, and normal-slip solutions could fit the same first motion data.

An alternative approach to estimate source mechanisms and principal moment orientations is to use a waveform inversion method to estimate seismic moment tensors of microearthquakes at The Geysers. The frequency domain method of Stump and Johnson (1977) is used here to estimate second-order moment tensors for three microearthquakes at The Geysers geothermal field. A goal is to determine the utility of waveform moment tensor inversion to supplement P-wave first-motion data, when they are of insufficient quantity and distribution to constrain microearthquake focal mechanisms. The primary utility of the moment tensor inversion approach in this context is to obtain well constrained focal mechanism estimates using full waveform data from a limited number of stations.

We also wanted to determine the reliability of microearthquake waveform moment tensor inversion results. Saikia and Herrmann (1986) could not independently verify the accuracy of waveform moment tensor inversion for Arkansas microearthquakes because first-motion data were only available from a small number of stations. The large number of P-wave first motions available for

microearthquakes at The Geysers provide sufficient focal mechanism constraints to check waveform moment tensor estimates for two of the earthquakes.

In contrast to teleseismic and regional geometries, microearthquake mislocation can produce substantial errors in distances, azimuths, and take-off angles used to calculate Green functions. An appraisal methodology is developed to quantify the effects of these components of Green function errors and velocity model errors on moment tensor decompositions. We begin by outlining the source characterization and moment tensor inversion method used. Next, the data set and details of the inversions are presented. The moment tensor error appraisal method is then presented and applied to the results of moment tensor inversions.

2. Source Characterization

The moment tensor formulation is used to represent the seismic source in space and time. Utilizing the fact that a seismic source can be represented as a set of equivalent body forces, the source can be expanded as a series of moments. For small sources or large wavelengths, only the first term of the series is retained (point source approximation), and the displacement at any point and time can be written as

$$U_k(\underline{x}',t') = G_{ki,j}(\underline{x}',t';\underline{0},0) \circledast M_{ij}(\underline{0},t') \tag{1}$$

where U_k is the displacement in the k direction, G_{ki} is the Green function, M_{ij} is the moment tensor, $_{,j}$ indicates differentiation with respect to x_j, and $\circledast$ represents temporal convolution. A more complete derivation of (1) is given in Stump and Johnson (1977).

In the frequency domain, equation (1) reduces to

$$U_k(\underline{x}',f) = G_{ki,j}(\underline{x}',f;\underline{0},0) \cdot M_{ij}(\underline{0},f) \tag{2}$$

If the propagation paths effects $(G_{ki,j})$ are known, one can determine the source (M_{ij}) from a set of observational data (U_k) by solving this set of linear equations.

In the implementation used here, Fourier transforms of the data and Green functions are calculated, and the moment rate tensor $(\dot{M}_{ij})$ is solved for in the frequency domain. An inverse Fourier

40

transform is used to obtain $\dot{M}_{ij}$ in the time domain. Then $\dot{M}_{ij}$ is detrended to eliminate spurious dc offsets. The resulting estimates of $\dot{M}_{ij}$ are integrated to yield M_{ij}. Detrending of $\dot{M}_{ij}$ is physically justified because the moment rate tensor elements cannot have a permanent dc offset. If perfect data were available, detrending would not be required but all seismic data are intrinsically bandlimited, and the instruments used here (4.5 Hz velocity transducers) have limited low frequency responses. Detrending as applied, is simply a high-pass filter operation to remove spurious low frequency (< 1 Hz) noise.

Since the complex frequency dependence is obtained for each moment tensor element, moment tensor elements are not required to have a common time function. This allows inversion for complex sources that could have several physical source components with different time histories. An alternative approach is to solve for the moment tensor element time functions using the multichannel vector decomposition method developed by Oldenburg (1982), as presented by Sipkin (1982). In cases with source multiplicity, allowing all moment tensor elements to have their own time functions eliminates errors in moment tensor estimates that are inherent in time domain approaches that assume a common time function for all moment tensor elements (see Sipkin (1986) for some examples).

The moment tensor characterization of seismic sources provides a means for estimating source properties of microearthquakes. Stump and Johnson's (1977) approach is completely general; no restrictive assumptions are required about physical source types or the time dependence of moment tensor elements. All physical source types can be analyzed including isotropic (volume) sources, compensated linear vector dipole (CLVD) sources, and double-couple sources. Any of these source types can be investigated using graphical first-motion methods by relaxing the common double-couple source assumption. However, the linear programming moment tensor inversion method of Julian (1986) provides the most powerful means to utilize first-motion data.

The primary advantage of the using moment tensor waveform inversion in conjunction with first motion information is that fewer recording stations are needed to constrain seismic source properties. Only 6 components of ground motion (two three-component stations) are required in theory, although in practice about 15 components of ground motion are recommended to ensure reliable results. Another advantage is that azimuth and takeoff angle coverage need not be as comprehensive as when only P-

41

wave first-motion data are utilized. Consequently, it is possible to constrain source properties of earthquakes that are not completely surrounded by recording stations, something that is not generally possible when using only P-wave first motion data.

Frequency domain moment tensor inversion has not been applied to microearthquakes before. Stump and Johnson (1984) have used the method to characterize nuclear explosion sources using near-field data. Time domain moment tensor inversions with restrictions on physical source type (pure deviatoric) and moment tensor time dependence have been applied to microearthquake data by Saikia and Herrmann (1986). However, their approach requires assuming that all moment tensor elements have the same time function and that the time function is known or can be estimated. The result of this type of inversion is a static estimate of the moment tensor elements. Since the source time function is intrinsically unknown, any errors in the assumed time function will produce errors in the static moment tensor estimate. Further, if all moment tensor elements do not actually have the same time function, another component of error will be added to the static moment tensor estimate. The approach used here allows each moment tensor to have an independent time function. This requires more data than the time domain approach of Saikia and Herrmann (1986), Langston (1981), and Langston and Helmberger (1977), but yields more complete information about source properties.

Estimated moment tensors can be decomposed into isotropic and deviatoric components. The relations are

$$M_{TR} \text{ (isotropic)} = \frac{1}{3} M_{ii} \tag{3}$$

$$D_{ij} \text{ (deviatoric)} = M_{ij} - M_{TR} \delta_{ij}. \tag{4}$$

If prior knowledge is available about the source, then appropriate constraints can be placed on equation (2). Constraints on equation (2) were not used when inverting for microearthquake moment tensors. Non-double-couple earthquake mechanisms cannot be excluded at The Geysers. Consequently, we wanted to investigate if unconstrained moment tensor inversions would produce moment tensor estimates consistent with the common assumption for earthquakes of a single double-couple source. The frequency domain approach was used to avoid errors due to possible source multiplicity. The point

42

source assumption is valid for the microearthquakes used here, since source dimensions are small compared to the wavelengths represented in the observed data.

The eigenvalues and corresponding eigenvectors of D_{ij} describe the magnitude and orientation, respectively, of the principal moment axes (neglecting gravity) acting at the source . These principal moment axes represent the quantity that is uniquely determined (within a range of uncertainties due to errors in U_k and $G_{ki,j}$) by moment tensor inversion. Decomposition of D_{ij} into physical source components is fundamentally nonunique (Geller, 1976). Julian (1986) used linear-programming methods to investigate the range of possible physical source mechanisms that are consistent with a particular first-motion or amplitude data set. The common approach of decomposing D_{ij} into double couple and CLVD components is not particularly meaningful due to its intrinsic nonuniqueness unless it is believed that both components are truly contained in the seismic source. A simple shear dislocation earthquake source can have nonzero CLVD components if the rupturing fault plane has nonzero curvature and a nonzero isotropic component if a fault surface is irregular or imbedded in an anisotropic material (Backus and Mulcahy, 1976). The decomposition of D_{ij} into CLVD and double couple components does give a measure of the departure of the estimated source from a planar faulting single double-couple earthquake model. A simple measure of the departure of D_{ij} from a single double couple is the ratio of the smallest and largest eigenvalues of D_{ij}.

A simply relationship does not exist between principal moment and principal stress orientations. The maximum principal stress orientation is poorly resolved by the principal moment orientations (McKenzie,1969). Principal moment estimates from many earthquakes can be incorporated into stress tensor inversions (Angelier, 1984; Gephart and Forsyth, 1984; and Michael, 1987). Oppenheimer (1986) used the method of Angelier (1984) to estimate principal stress orientations at The Geysers using focal mechanism data. Michael (1987) demonstrated that principal moment orientation data can provide sufficient information to find the best stress tensor, albeit at decreased resolution compared to using slickenside or known fault orientation data.

3. Data Analysis

A 9 station three-component digital seismometer network was deployed in The Geysers from July 21 to August 15, 1982. The network was located entirely inside the geothermal production zone to avoid the effects of significant lateral velocity variations (Eberhart-Phillips, 1986) outside this zone. A complete description of the recording network and data can be found in O'Connell (1986). Data were recorded at 200.32 samples/sec using three-component 4.5 Hz velocity-transducer geophones. Before sampling, the data were anti-alias lowpass filtered using a 5- pole Butterworth filter with a 50 Hz corner frequency and high pass filtered with two 1-pole Butterworth filters with 0.2 Hz corners. The rapid decrease of displacement magnification of the velocity transducers below 4.5 Hz, combined with the 12-bit resolution of the recording system, limited the usable frequency band to the range from 1.0 to 50 Hz. Also, electrical problems with some of the recorders resulted in increased noise at low (<1 Hz) frequencies, so moment tensor estimates below 1 Hz are unreliable. This does not significantly effect the results of the moment tensor inversions because source corner frequencies for the microearthquakes used here are between 6 and 10 Hz. It does however, necessitate detrending of the moment rate tensor in the time domain, as discussed earlier.

The maximum observed corner frequencies at The Geysers is strongly correlated with particular station sites. Certain stations consistently produced lower corner frequencies and larger high frequencies rolloffs, independent of epicentral distance or hypocentral depth. This strongly suggested that an f_{max} effect (Hanks, 1982) was controlling the maximum observed corner frequencies at some stations. An f_{max} of 15 to 20 Hz was observed for station sited on slope failure materials. To reduce problems associated with variations of f_{max} as a function of station site, the data were lowpass filtered using a 2-pole Butterworth filter with a 10 Hz corner frequency. This also decreased the burden of Green function computations by reducing the maximum frequency required. The price paid is that moment tensor time functions represent lowpass-filtered versions of the true source time functions.

Green functions were calculated using a spectral wavenumber-frequency approach similar to the reflectivity method of Kind (1978). The entire model between the free surface and the model bottom constitutes the reflectivity zone; all reverberations, including free surface reflections, are included. The

44

resulting Green functions represent the complete medium response. Since the wavenumber response is computed as a function of frequency, the frequency-domain Green functions used in equation (2) are obtained directly.

The P and S-wave velocity models estimated for The Geysers in O'Connell (1986) from a P and S-wave progressive velocity-hypocenter inversion are used in Green function calculations and are shown in Figures (1) and (2). The velocity models used in a feasibility study of moment tensor inversion at The Geysers are also shown in Figures (1) and (2). The initial velocity model does not appear to be greatly different from the final model. However, moment tensor inversions with the initial model failed to produce the correct amplitude pattern of P and S-wave phases on any components of ground motion, in contrast to the results obtained using the final velocity models (Figure (7)). The progressive P and S-wave velocity-hypocenter inversion constituted an essential component of the moment tensor inversion process.

Anelastic attenuation was included by specifying a Q model for The Geysers consistent with the results of Majer and McEvilly (1979). Values of 50-100 were used for Q_P, and values of 40-80 were used for Q_S. The low Q values were used near the free surface and the higher values used in the production zone. These low Q values reflect the combined effects of intrinsic attenuation and scattering losses and correspond to effective Q values.

Proper phase matching of observed S-P times with Green function S-P times is important to ensure the success of the moment tensor inversions. Earthquake locations estimated in O'Connell (1986) were used to define initial hypocenter-receiver azimuths and distances. Since recording station were located at different elevations, the predicted S-P times for initial hypocenter-receiver distance did not always match observed S-P times. Hypocenter-receiver distances were modified so as to produce correct Green function S-P times. Hypocenter- receiver azimuths are preserved but takeoff angles are somewhat different. For one station take-off-angles were altered by as much as 29° for one event, but for most stations take-off-angles were not changed by more than 5° - 15°. Table (1) contains the minimum and maximum take-off-angle error ranges, and mean take-off-angle errors and their standard deviations for all events.
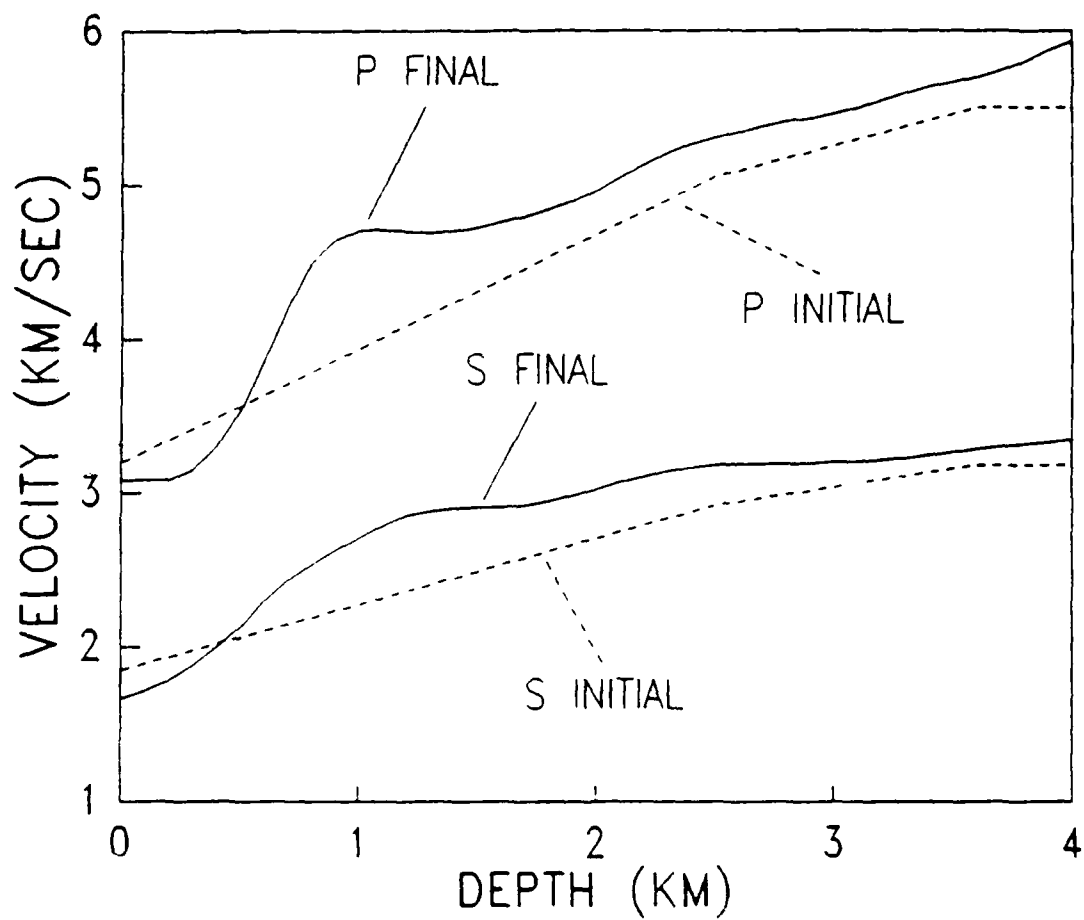
Figure 1. P and S-wave velocity models used for a feasibility study of moment tensor inversions at The Geysers (denoted as initial) and the models used for the final moment tensor inversion (denoted as final). Note that the initial P and S-wave velocity models have overall velocity gradients similar to the final models.
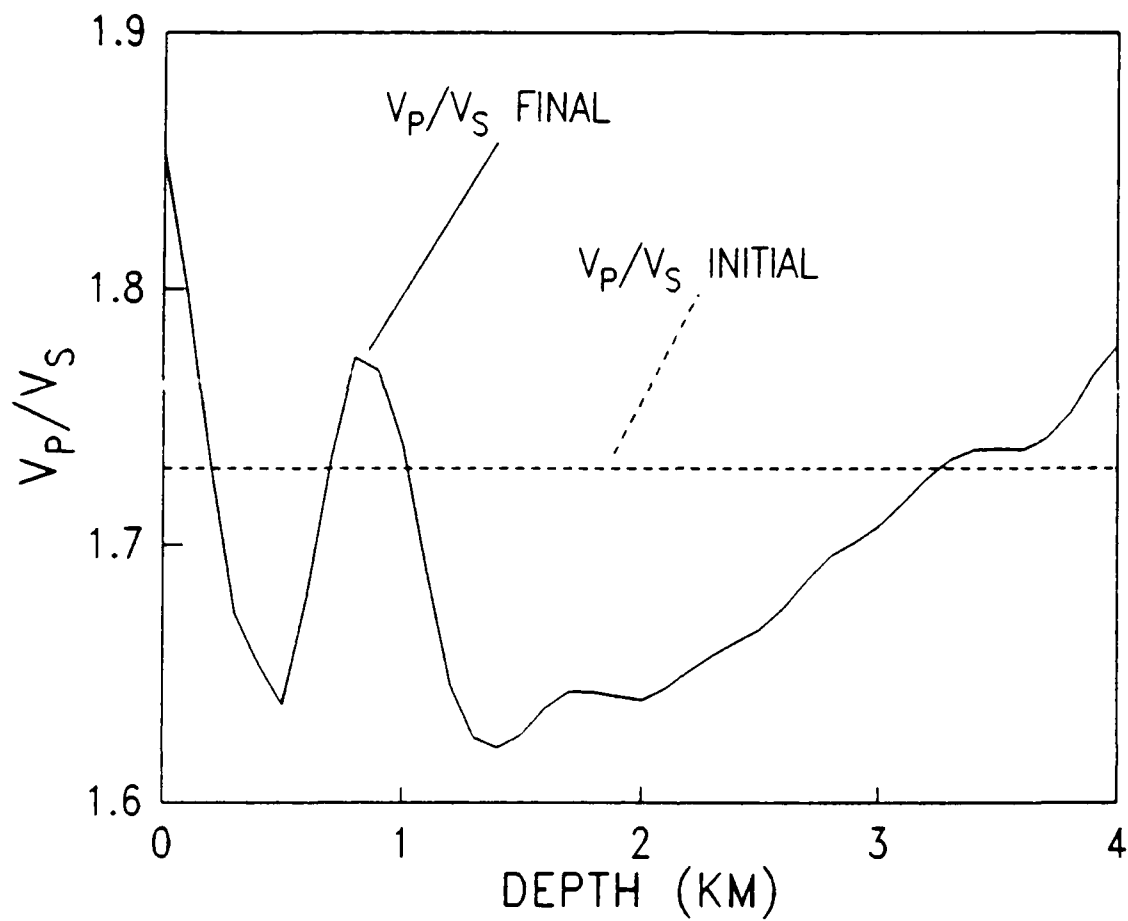
Figure 2. V_P/V_s initial and final models used in real and synthetic waveform moment tensor inversions. Note that the assumption of constant V_P/V_s used in the initial model is clearly in error.

Since a frequency domain inversion is used, it would be difficult to use windows about certain phases in the inversion. Small time windows about the first P and S-wave pulses would not provide the frequency bandwidth or resolution needed to reliably estimate the moment tensor. Truncation effects due to windowing are accentuated for short time windows. Consequently, complete seismograms were used for all components in inverting for the moment tensor. Ten seconds of data were used in the inversions. For stations that had shorter records, zeros were added to give total lengths of 10 seconds.

While record lengths of 10 seconds were used in the moment tensor inversions, moment tensor results are plotted for times less than one second. This was done because source durations are short, approximately 0.1 sec and because the Green functions do not contain coda wave durations as long as seen in the observed data. Also, some components of the observed data had small noise glitches approximately two seconds after the first S-wave arrival and these glitches contaminate the moment tensor time functions after several seconds. Windows of less that one second were used to detrend the moment rate tensor. Since the source durations of these microearthquakes were short, this approach is reasonable.

Take-off-angle Errors				
Event	Range		Mean	SD
	min	max		
1	-16°	27°	-1.2°	11.5°
2	-16°	-1°	-8.1°	5.5°
3	-29°	1°	-15.6°	9.8°

Table 1. Combined P and S-wave first arrival take-off-angle errors for all events, defined as the difference between progressive inversion estimates and Green function estimates.

4. Inversion Results

Moment tensor inversions were done for three earthquakes at The Geysers. Two of the events were shallow, approximately 2 km below the mean station elevation, and the third event was deeper, approximately 4 km below the mean station elevation. The shallow events correspond to the depth interval where the strike-slip, normal-slip, reverse-slip ambiguity is most pronounced. Oppenheimer (1986) found that most events in this depth range had strike-slip solutions with a smaller number of events having reverse-slip mechanisms. The deeper event corresponds to the depth interval where normal faulting mechanisms predominate (Oppenheimer, 1986).

Event and station locations are shown in Figure (3). Events 1 and 2 have a range in epicentral distances representing first arrival take-off angle coverage over 45°, but also have a large azimuthal gap in station coverage to the south. Conversely, event 3 has excellent azimuthal coverage, but very limited take-off angle coverage. All event inversions were full rank, with the condition numbers for the event 3 inversion about twice those of the event 1 and 2 inversions over the frequency band 2-20 Hz. The larger condition number for event 3 reflects a near linear dependency due to the limited take-off angle coverage. Consequently, the event 3 inversion is most likely to be adversely affected by errors in the data or Green functions.

Results of the moment tensor inversion are displayed in the following manner. The orientations of the eigenvectors of D_{ij} are plotted on stereographic lower hemisphere projections along with available P- wave first motion data. The P-wave first motion data come from the temporary network and USGS stations. In order to obtain as many first motions as possible, USGS stations outside the primary production zone at The Geysers were used. The P-wave velocity model estimated in O'Connell (1986), is not completely adequate to determine azimuth and takeoff angles for stations outside The Geysers for two reasons. Firstly, P-wave velocity estimates from the progressive velocity- hypocenter inversion are only available to a depth of 4.0 km and more distant station arrivals correspond to rays bottoming below this model depth, in a part of the model that was added as a rough estimate of the velocity structure below 4.0 km. Secondly, Eberhart-Phillips (1986) has found significant lateral variations of P-wave velocity structure outside The Geysers production zone, so azimuthal estimates may be in error for

49
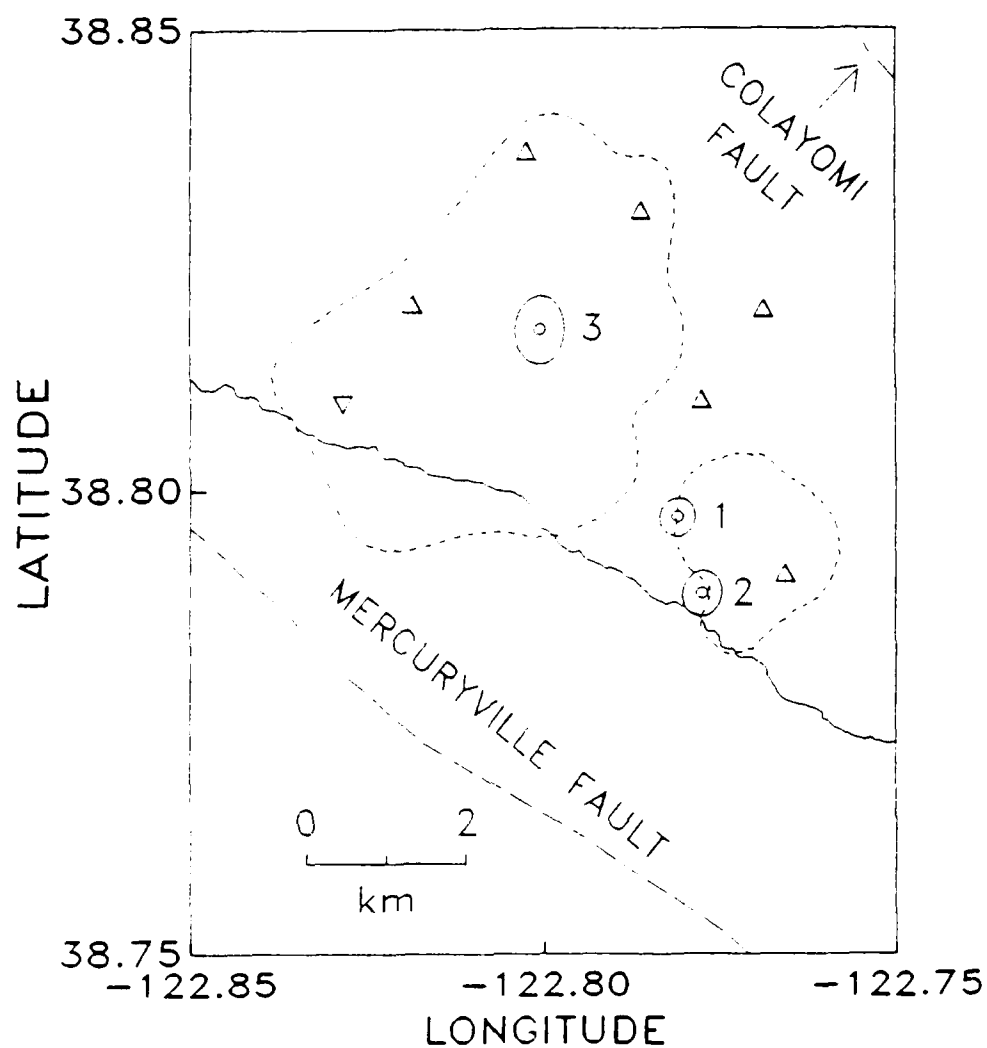
Figure 3. Map showing relation of earthquake epicenters (circles with event numbers on the right) to stations (Δ and ∇) used in moment tensor inversion. The station denoted by the ∇ was not used for Event 2. Hypocentral depths and standard errors for events 1, 2, and 3, where 1.4 ±0.1, 1.6±0.2, and 3.5±0.1 km, respectively. Ellipses represent two-standard-deviation epicentral error estimates. The solid trace is Big Sulfur Creek. The fine-dashed lines are 34.5 bar contours (Lipman et al., 1978) enclosing areas of pressure decline for the year 1977 and provide a rough outline of The Geysers' primary steam production zones.

USGS stations well outside The Geysers due to lateral refraction. The estimated position of first motions on the focal sphere of the distant (> 20 km) USGS readings may have substantial uncertainties.

Inversion results are summarized in Table (2) and Figures (4-6) for events 1, 2, and 3, respectively. The estimated principal stress orientations for these three Geysers earthquakes prove to be quite stable (Figures (4-6)), and provide results consistent with observed P-wave first motion distributions. The decompositions of the estimated moment tensors into isotropic and deviatoric components show small to moderate departures from a single double-couple source for events 1 and 2 and large ones for event 3 (Table (2)). The sometimes large isotropic component for event 3 can be partially explained by instability of the M_{zz} component due to the aforementioned take-off angle problem. However, it is not immediately clear how to interpret the apparent source mechanism complexity in light of potential sources of error in the Green functions, such as the take-off angle errors listed in Table (1), source mislocation, and velocity model errors. In an effort to quantify the effects of Green function a series of synthetic tests were done and are described in the next section. Consequently, we defer further interpretation of the moment tensor estimates to a latter section in order to incorporate the synthetic test results.
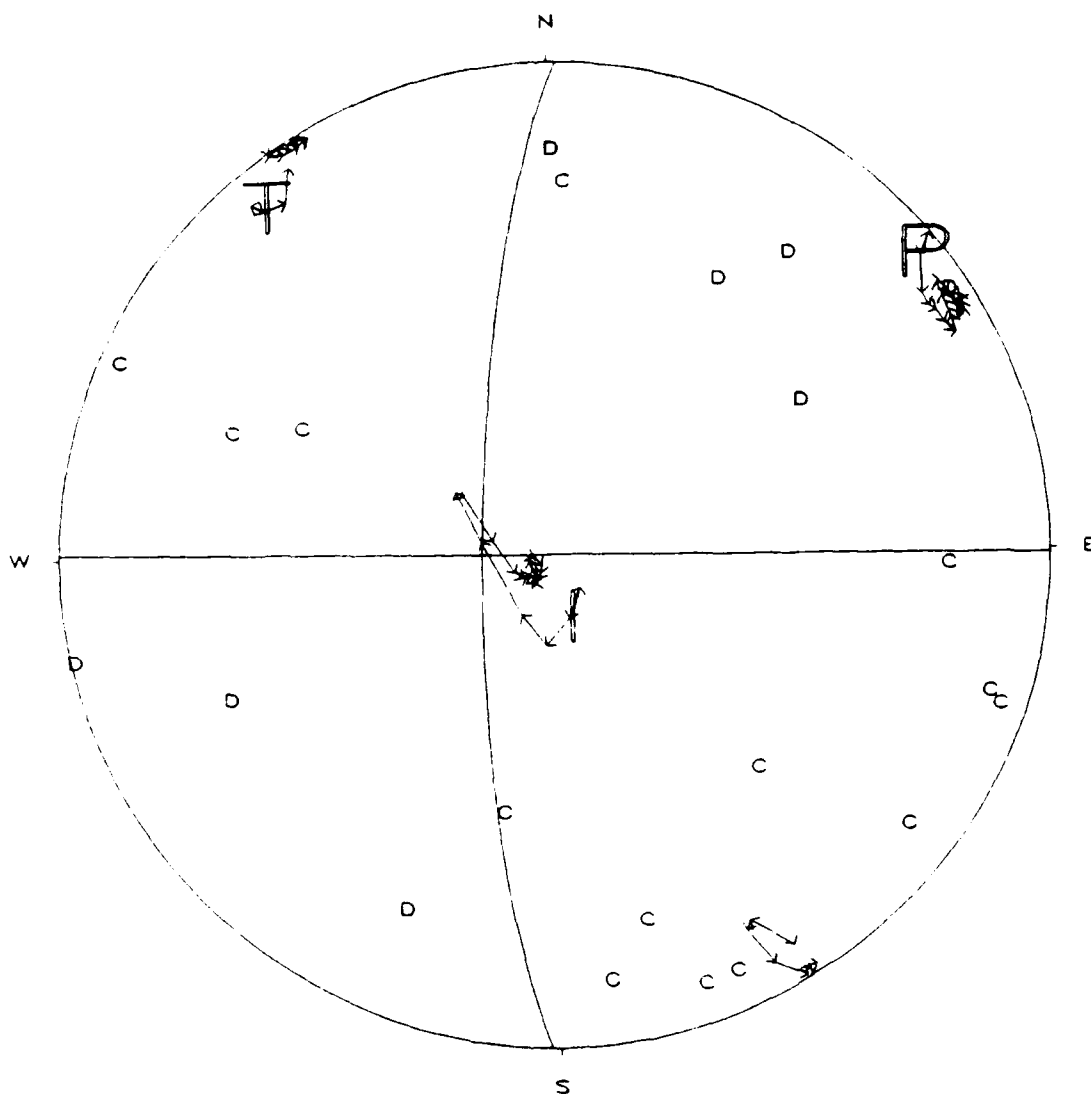
Figure 4. Lower-hemisphere equal-area plot of P-wave first motions, time varying principal moment axes (0.5 second duration) estimated from the moment tensor inversion, and double-couple fault plane solution for event 1. Compressional and dilatational P-wave first motions are plotted as (C and +) and (D and -), respectively. The tension axis is denoted by the large (T) and its time history is shown as line segments with arrowheads pointing toward the next point in time. The compression axis is denote by a large (P) and the intermediate axis is denoted by a large (I). The solid lines are nodal planes drawn to satisfy the first motion data. The inconsistent compression in the upper right quadrant corresponds to a distant station and its position has large uncertainties due to lateral refraction effects.

52

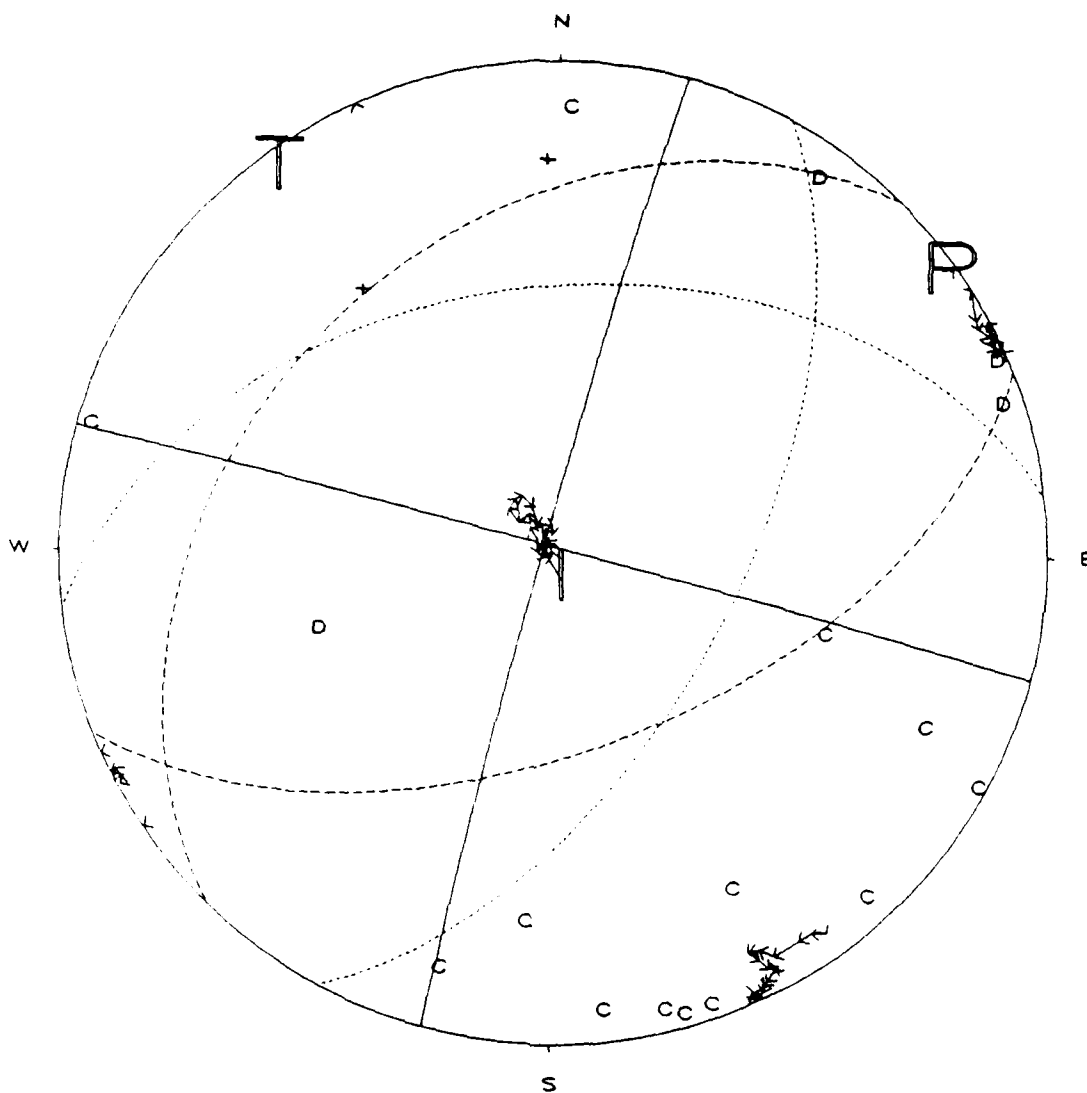**Figure 5.** Principal moment axes (0.5 second duration) and focal mechanism for event 2 with same convention as Figure (4). The short-dashed line nodal planes represent two other solutions compatible with the first motions.

53
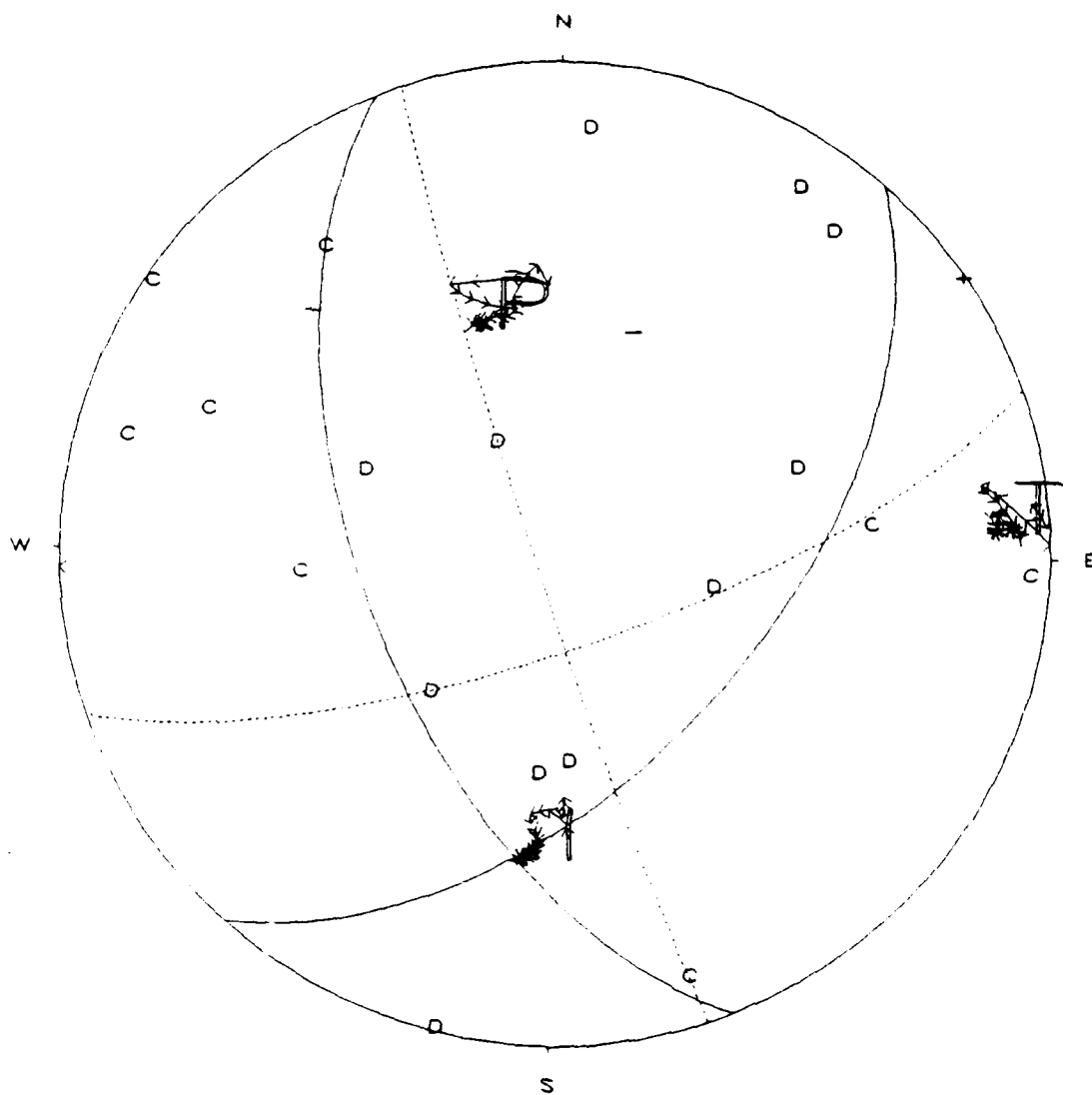
Figure 6. Principal moment axes (0.8 second duration) and focal mechanisms for event 3 with same convention as Figures (4 and 5).

Moment Tensor Inversion Summary										
Event	Sta.	Comp.		M_c	M_o	Isotropic		CLVD		τ
		V	H			min	max	min	max	(sec)
1	7	7	14	1.6	0.2	0	15	10	40	0.5
2	6	6	11	1.8	0.8	10	25	10	20	0.5
3	7	7	10	2.3	3.0	10	55	0	40	0.8

Table 2. Moment inversion information by event number showing the number of stations and ground motion components used, V for vertical and H for horizontal. M_c is U.S.G.S coda magnitude, M_o is scalar moment in units of 10^{20} dyne-cm. The last 5 columns represent minimum and maximum isotropic percentages of the total moment, minimum and maximum CLVD percentages of the deviatoric moment, and τ is the moment time duration used for these estimates.

5. Synthetic Tests

The formulation for solving for the moment tensor presented in equations (1-2) assumed that Green function errors were insignificant. Using matrix notation, a solution for the moment tensor elements, m, is written

$$m = G^{-1}u \qquad (5)$$

where G^{-1} is the inverse Green function and u are the measured ground motion data. Moment tensor inversion approaches which assume that errors only occur in the ground motion data, u, will underestimate errors in moment tensor estimates and their eigenvalue-eigenvector decompositions. A more realistic representation is to rewrite (5) in the form

$$M = f(G^{-1},u) \qquad (6)$$

to emphasize that G is also an unknown to some degree. We investigate the mapping of uncertainties in G into estimates of M by determining estimates of M for a suite of extremal values of G using (5). The effects of Green function errors can be assessed from the resulting variation of M estimates thus obtained.

For microearthquakes the primary sources of Green function error are earthquake mislocation and incorrect velocity structure. Source mislocations effects are significant because stations are close to epicenters, producing Green function errors due to incorrect distances, azimuths, and take-off angles. Incorrect velocity models produce amplitude and take-off angle errors in calculated Green functions.

The synthetic tests focus on source mislocation effects, although a preliminary effort to appraise velocity model error effects is included. There are two reasons for focusing on mislocation effects. Firstly, realistic estimates of hypocentral uncertainties for the three Geysers events are available from a progressive velocity-hypocenter inversion (Eberhart-Phillips, 1986; O'Connell, 1986) and a nonlinear hypocentral error appraisal (O'Connell, 1986). Secondly, although velocity models have been determined for the Geysers (Eberhart-Phillips, 1986; O'Connell, 1986), the intensive computational requirements of completely appraising velocity model errors is beyond the scope of the present investigation.

The 95% confidence ellipses from O'Connell (1986) for the epicentral locations of all three events are shown in Figure (3) and 95% confidence hypocentral depth uncertainties are presented in Table (3). Eberhart-Phillips (1986) noted that a one-dimensional velocity-hypocenter inversion with station corrections (the method used in O'Connell, 1986) produce epicentral estimates close to those obtained using a three-dimensional velocity-hypocenter inversion. However, a possibility of a systematic epicentral bias exists; epicentral uncertainties may be a factor of two larger. Consequently, synthetic error estimates reflect the minimum error that could be attributed to hypocentral mislocation at a 95% confidence level.

The double-couple mechanisms determined from the moment tensor inversions and first-motion data (solid nodal lines in Figures (4-6)) were used to define the "true" source mechanisms of the three events in the synthetic tests. The "true" synthetic waveform data were generated using these source mechanisms, the "final" velocity models in Figure (1), and the "correct" hypocenters. Simple double-couple source mechanisms were used to determine what percentage of spurious isotropic and CLVD components could be produced simply by using incorrect earthquake locations and/or incorrect velocity models. The same stations and ground motion components used in the real data inversions were used in the synthetic inversions.

To determine the effects of mislocation errors, moment tensor inversions were done using Green functions calculated using hypocentral positions on the 95% confidence error ellipsoid. The combined effects of mislocation and velocity model errors were investigated by using the initial velocity models in Figure (1) to calculate the mislocation Green functions. This approach was implemented using the WKBJ method (Dey-Sarkar and Chapman, 1978) to calculate the Green functions since all potential first arrivals represented upgoing ray paths. Because many values of G must be computed, the WKBJ method was chosen for its combination of accuracy and computational efficiency. To further reduce the computational burden, known source time functions were assumed, allowing time domain inversions for the static moment tensor. Eight point time windows beginning at the first P and S-wave arrivals were used in the inversions. In contrast to inversions with real waveform data, the waveform data are error free in the synthetic tests.

57

Specific results of particular synthetic tests cannot be generalized because they depend on source-receiver geometry and source mechanism. At a fixed source-receiver geometry changing the source mechanism will produce a different radiation pattern relative to the station distribution on the focal sphere. Similarly, for a fixed source mechanism one station distribution can be more prone to errors than another. Consequently, moment tensor error characteristics need to be investigated on a event by event basis.

Synthetic Results								
Event	Δz	GF err.	Isotropic		CLVD		P	T
	(km)		min	max	min	max	max	max
1	0.20	misloc.	0.1	0.7	0.0	0.5	0.4°	0.1°
		+vel.	0.2	9.5	10.6	14.7	7.6°	6.7°
2	0.27	misloc.	0.0	2.3	0.5	7.7	0.6°	1.3°
		+vel.	9.5	14.3	18.6	26.5	5.6°	5.4°
3	0.23	misloc.	0.0	2.4	0.0	7.7	1.1°	0.8°
		+vel.	4.0	7.0	5.7	13.9	2.7°	1.4°

Table 3. Synthetic moment tensor inversion test results by event number showing ranges of spurious

isotropic and CLVD component percentages and maximum P and T axis errors. For each event, results

are listed for the cases of mislocation and combined mislocation and velocity model Green function

errors. Maximum depth mislocations are listed as Δz (see Figure (3) for epicentral mislocations).

Results of the synthetic tests are summarized in Table (3). Essentially the same results were obtained when a zero isotropic constraint was used and are therefore omitted. The results listed in Table (3) represent a lower error limit for the source-receiver geometry considered. Overall errors for real data moment tensors inversions would be larger due to the combined effects of Green function errors and statistical errors in the data.

Errors in P and T axis positions are relatively smaller than errors in the physical source decomposition into isotropic, CLVD, and simple double couple. The results of these and other synthetic tests indicate that principal moment axis orientations are much less sensitive to mislocation and velocity model Green function errors than the physical source decomposition into isotropic, CLVD, and simple double-couple components. This result make intuitive sense because a variety of physical source components can be assembled that are consistent with a particular set of principal moment orientations and produce certain level of misfit to the observed data. For instance, adding small spurious isotropic source components might compensate for systematic underestimation of P-wave amplitudes due to a systematic Green function error. Yet, the principal moment axis orientations will be unaffected.

The waveform misfits produced by using incorrect velocity models and hypocenters to calculate Green functions were small. The erroneous isotropic and CLVD components effectively compensated for Green function errors to yield small waveform misfits. For the source-receiver geometries of these events, small waveform misfits alone were not a reliable indicator that moment tensor errors were small.

6. Discussion

From Table (3) it is clear that moment tensor decomposition errors due to mislocation alone are small for these three events, although small spurious CLVD percentages were obtained for event 2 and 3. When velocity model errors are combined with locations errors, the spurious isotropic and CLVD components are large enough to explain the sizes of the isotropic and CLVD components obtained for events 1 and 2 using real data. A portion of the CLVD component for all events may be caused by distortion of a dominantly quadrapole radiation pattern due to lateral velocity heterogeneity.

The larger isotropic and CLVD components estimated for event 3 may reflect poorer velocity resolution in the progressive-velocity hypocenter inversion since the source depth is located in the deepest, least resolvable portion of the estimated velocity model. Alternatively, there is no reason to assume *a priori* that the larger isotropic and CLVD component estimate for event 3 might not reflect a true source property. The deeper seismicity at The Geysers appears to delimit the lower boundaries of the steam field and appears to have predominantly normal-faulting mechanisms (Oppenheimer, 1986). The large CLVD component for event may indicate tensile failure is occurring at the base of the steam field. Tensile failure has been inferred at another geothermal field by Foulger and Long (1984). However, Foulger and Long clearly delineated a strong non-quadrapole radiation pattern from events with a comparable distribution of first-motion data, but the first-motion data of event 3 is compatible with a quadrapole radiation pattern (Figure (6)). Thus, known and potential errors in the assumed Green functions, and the unfavorable source-receiver geometry for event 3 probably produced substantial spurious isotropic and CLVD components. Further refinements of the moment tensor inversion approach and improved Green function calculations will be required to determine the significance of the isotropic and CLVD components of event 3.

Since none of the deviatoric moment tensors corresponds to a single double-couple for the entire moment duration, the P-wave nodal surfaces will not correspond to orthogonal planes for the entire moment duration. However, results of the synthetic tests indicate that significant deviations from single double-couple source mechanisms cannot be resolved for these three events. Further, there is no evidence from the P-wave first motion distributions for significant deviations from a quadrapole radiation pattern. Consequently, in the following analysis we assume that a simple double-couple source mechanism is an appropriate approximation to interpret the deviatoric moment tensor.

The P-wave first motions for events 1 and 3 provide sufficient constraints to unambiguously resolve the focal mechanism (Figures (4) and (6)). The estimated principal moments orientations for events 1 and 3 are in excellent agreement with the first motion focal mechanism solutions. These results bear out the synthetic test conclusions that principal moment orientation estimates are robust with respect to Green function errors. Note that, if the north-most and west-most dilatations were

61

unavailable in Figure (4), a normal faulting mechanism would be compatible with the remaining P-wave first motions. The moment tensor solution provides sufficient information to resolve the correct focal mechanism and required waveform information from only 7 stations. In contrast, 21 P-wave first motions were required to constrain the nodal planes in Figure (4).

For event 2 the principal moment positions are used as constraints to construct the "best" focal mechanism, using the P-wave first motions as the additional constraints (Figure (5). The fault plane solutions shown in Figure (5) demonstrate that a wide range of focal mechanisms are consistent with the P-wave first motion data. Solutions ranging from nearly pure normal-slip to pure strike-slip are consistent with the first motion data (Table(4)). The moment tensor solution constrains the solution to be dominantly strike-slip. The orientations of the principal moment axes are stable even though there is a large azimuthal gap in station coverage.

Event 2 is the type of earthquake that made Oppenheimer's (1986) reduction of his fault plane solution data difficult. The P-wave first motions are consistent with both strike-slip mechanisms (postulated shallow event mechanism) and normal-slip mechanisms (postulated deep event mechanism). He would have been forced to discard this event because constraints are absent with respect to the depth-dependent-focal-mechanism hypothesis. The moment tensor waveform inversion method provided sufficient resolution to distinguish the appropriate focal mechanism using data from a subset of stations.

The fault plane solution in Figure (6) is constrained by three first motions, the two west-most dilatations, and the northeast compression shown as (+). If these 3 first motions were unavailable, an almost pure strike-slip mechanisms would fit the first motion data. These three first motions would not be available for a USGS solution, since the dilatations represent temporary station readings, and the (+) is an ambiguous reading from a distant station. The full first-motion data set confirms the moment tensor P and T axis estimates for event 3 and demonstrates that comparable focal mechanism resolution can be achieved with the waveform inversion using data from 7 stations, instead of the 22 first-motions required to constrain the focal mechanism in Figure (6).

| P and T Axis Orientations								
	First Motion				Waveform			
	P		T		P		T	
Event	trend	plunge	trend	plunge	trend	plunge	trend	plunge
2131638	47°	2°	133°	14°	50°,62°	0°,10°	145°,150°	-10°,20°
2181937	59°	0°	149°	5°	53°,64°	-2°,3°	142°,154°	-4°,11°
	18°	72°	132°	11°				
2200908	355°	52°	92°	5°	338°,358°	40°,50°	80°,88°	-1°,14°

Table 4. Comparison of P and T axis orientations estimated from first-motion fault plane solutions and waveform inversions. The range of time variations of orientations of the principal moment axes are listed for the waveform moment tensor estimates. Event 2 has an ambiguous first-motion fault plane solution so two possible first motion solutions are listed.

7. Comparison of Observed and Predicted Seismograms

The earliest waveform moment tensor inversion attempts used the constant velocity layer parameterization model for The Geysers of Eberhart-Phillips and Oppenheimer (1984). Waveform amplitude predictions for P and S-wave phases were very poor even when the best moment tensors estimates obtained with the final model were used. The velocity discontinuities of the relatively thick (1.0 km) constant velocity layers produced phases arrivals that were more representative of parameterization than actual earth structure. The initial model in Figure (1) was produced as a linear velocity gradient modification and improved waveform amplitude predictions, but misfits were clearly unacceptable. However, when the final models (Figure (1-2)) of a progressive velocity-hypocenter inversion (O'Connell, 1986) were used, excellent agreement was obtained between relative P and S-wave first-arrival amplitudes for all inversions (Figure (7)). The primary differences between the initial and final models are reflected in V_p/V_s (Figure (2)) and larger velocity gradients near a depth of one kilometer for the final model. Agreement between observed and predicted seismograms using the final velocity model is very good for both P and S-wave first arrivals.

The initial models shown in Figure (1) are incorrect for The Geysers. They would be much closer to the estimated final models than a small set of constant velocity layers, a parameterization commonly employed to calculate Green functions for waveform studies of local events. The constant V_p/V_s assumption made for the initial model in Figure (2) was clearly wrong for The Geysers, but also reflects an assumption often made in waveform studies.

Saikia and Herrmann (1986) suggested that unsatisfactory S-wave synthetic fits from moment tensor waveform inversions for two Arkansas microearthquake were probably a reflection of inaccurate S-wave velocity models. Our experiences are consistent with their conclusions because waveform modeling deficiencies resulting from using the constant velocity layer and initial model parameterizations were very similar to those of Saikia and Herrmann (1986). These results reveal the importance of using realistic velocity models for microearthquake moment tensor inversions.
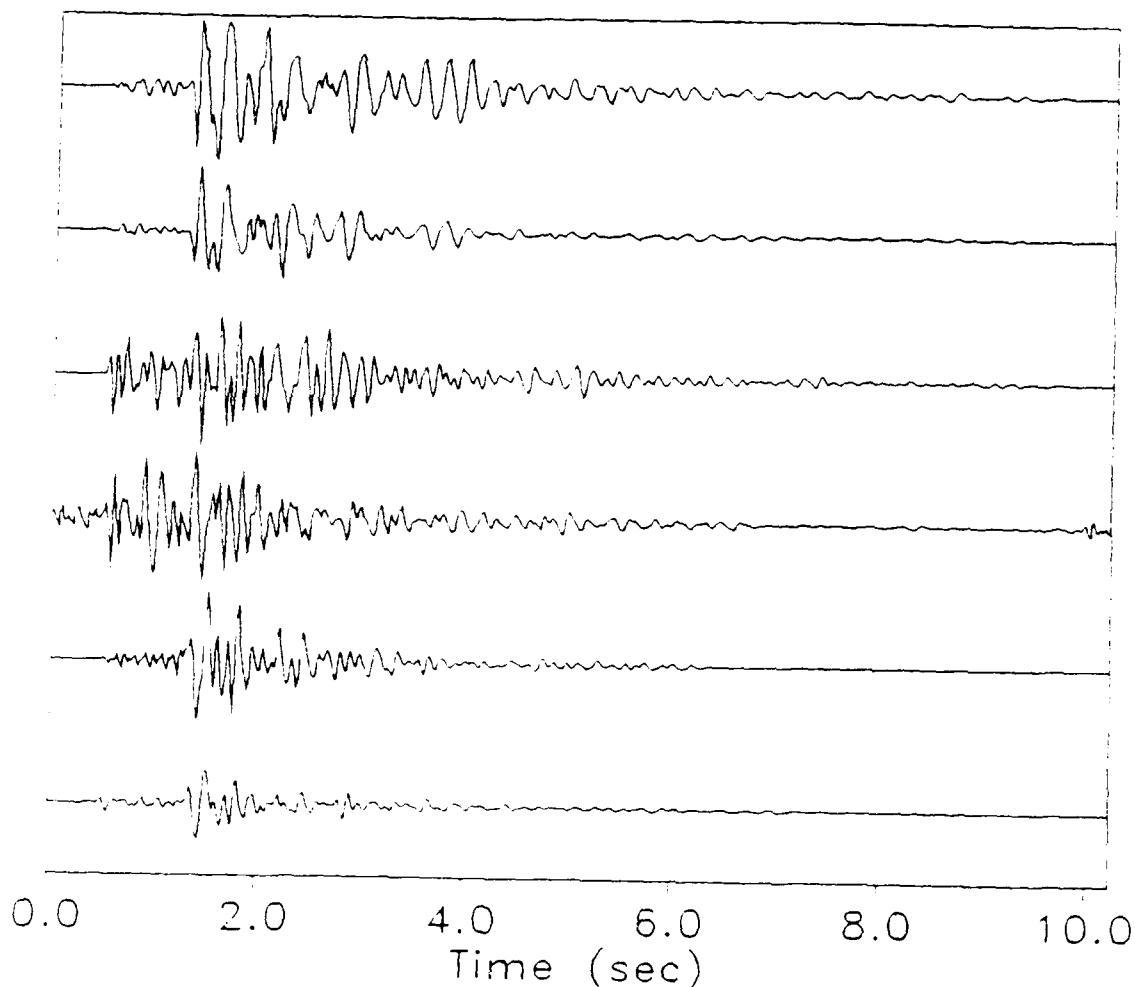
Figure 7. Three components of ground motion and corresponding synthetic seismograms from the moment tensor inversion for event 3. The synthetic seismograms are shown immediately below each observed data trace. The estimated moment tensor was convolved with the Green functions (calculated using the final velocity models) and the instrument response to produce the synthetic seismograms. The top two traces correspond to the real and synthetic east-west horizontal components of ground motion from station TPL, respectively, the middle two traces to the real and synthetic vertical components of ground motion at station TPL, respectively, and the bottom two traces to the real and synthetic north-south horizontal components of ground motion from station THR, respectively. Note that the relative amplitudes of the direct P and S-wave arrivals on all components of ground motion are faithfully reproduced in the synthetic seismograms.

8. Summary and Conclusions

Frequency domain moment tensor inversions were done for three microearthquakes from The Geysers geothermal field. The available first-motion data placed strong constraints on two microearthquake focal mechanisms. Waveform principal moment orientation estimates agreed with P-wave first motions focal mechanisms for these two events and constrained the focal mechanism of the event with ambiguous first-motion solutions. The moment tensor estimates of principal moment orientations were obtained using far fewer stations than required for first-motion focal mechanisms solutions.

The three focal mechanisms obtained here support Oppenheimer's (1986) hypothesis that focal mechanisms are a function of depth at The Geysers. Specifically, strike-slip focal mechanisms were obtained for the two shallow events and a predominantly normal-slip focal mechanism was obtained for the deep event, as his model predicts. The orientation of the T for the shallow events (events 1 and 2 in Table (1)) is rotated 40° to 50° clockwise, with respect to his estimate of 105° as the azimuth of least compressive stress for The Geysers. Since only two events are available for comparison the differences are probably not significant The potential of moment tensor inversions to provide well constrained principal moment orientations for individual events may make improve our understanding of the relationship between seismicity, steam production, and tectonic processes at The Geysers.

The results obtained here were dependent on reliable estimates of velocity structure so as to minimize errors in calculated Green functions. The velocity model determined in O'Connell (1986), when used in the moment tensor inversions, produced the correct ratio of P and S-wave amplitudes on all components of ground motion (Figure (7)). This result strengthens the arguments in O'Connell (1986) that the estimated models are good one-dimensional representations of the velocity structure at The Geysers.

The satisfactory results obtained here are a direct consequence of using P and S-wave data together to estimate velocity structure, hypocenter locations, and moment tensors. Although moment tensor inversions were not done to compare the effects of using just P-wave data to those using both P and S-wave data, Stump and Johnson (1977) found that inversions that just used P-wave maximum amplitudes were not as well conditioned as inversions using complete seismograms. It was clear from

66

the synthetic fits to the data, that the S-wave phases significantly constrained the moment tensor estimates.

Further improvements in assessing the effects of Green function errors on moment tensor estimates are needed. The synthetic tests presented here were used to roughly quantify Green function error effects. An obvious next step is to incorporate the methods used in the synthetic tests directly into real data moment tensor inversions. Modifications of the present moment tensor inversion procedure will allow elimination of take-off angle errors due to large station elevation differences. These improvements are required to resolve the significance of moderate amounts of isotropic and CLVD components contained in the microearthquake moment tensor estimates.

Conditions at The Geysers are similar to many geologically important areas of microseismicity. Consequently, The Geysers represents a good test of the feasibility of doing frequency-domain moment tensor inversions in geologically complex areas. Topographic variations are large, reflected in the 0.6 km variation of station elevations, near surface velocity variations are profound, and significant lateral velocity heterogeneities exist. These factors were not included in the moment tensor inversions, and useful results were obtained despite rather unfavorable station recording geometries for all three events considered. The real and synthetic data inversions demonstrate that, with the proper attention to determining realistic velocity structure and event locations, moment tensor estimates for microearthquake sources can be robust and provide a means to resolve source mechanisms using data from a relatively small number of stations.

Acknowledgements

References

Angelier, J., 1984. Tectonic analysis of fault slip data sets, *J. Geophys, Res.,* **89,** 5835-5848.

Backus, G. and Mulcahy, M., 1976. Moment tensor and other phenomenological descriptions of seismic source -II. Discontinuous displacements, *Geophys. J. R. astr. Soc.,* **47,** 301-329.

Bufe, C. G., Marks, S. M., Lester, F. W., Ludwin, R. S., and Stickney, M. C., 1981. Seismicity of The Geysers-Clear Lake region, *U. S. Geol. Surv. Prof. Pap. 1141,* 129-137. Dey-Sarkar, S. K., and Chapman, C. H., 1978. A simple method for the computation of body wave seismograms, *Bull. Seism. Soc. Am.,* **68,** 1577-1593.

Eberhart-Phillips, D., 1986. Three-dimensional velocity structure in Northern California Coast Ranges from inversion of local earthquakes, *Bull. Seism. Soc. Am.,* **76,** 1025-1052.

Eberhart-Phillips, D., and Oppenheimer, D. H., 1984. Induced seismicity in The Geysers geothermal area, California, *J. Geophys. Res.,* **89,** 1191-1207.

Eberhart-Phillips, D., 1986. Three-dimensional velocity structure in Northern California Coast Ranges from inversion of local earthquakes, *Bull. Seism. Soc. Am.,* **76,** 1025-1052.

Foulger, G. and Long, R. E., 1984. Anomalous focal mechanisms: tensile crack formation on an accreting plate boundary, *Nature,* **310,** 43-45.

Geller, R. J., 1976. Body force equivalents for stress-drop seismic sources, *Bull. Seism. Soc. Am.,* **66,** 1801-1804.

Gephart, J. W., and Forsyth, D. W., 1984. An improved method for determining the regional stress tensor using earthquake focal mechanism data: Application to the San Fernando earthquake sequence, *J. Geophys. Res.*, **89**, 9305-9320.

Hanks, T. C., 1982. f_{max}, *Bull. Seism. Soc. Am.*, **72**, 1867-1879.

Julian, B. R., 1986. Analyzing seismic-source mechanisms by linear-programming methods, *Geophys. J. R. astr. Soc.*, **84**, 431-443.

Kind, R., 1978. The reflectivity method for a buried source, *J. Geophys.*, **44**, 603-612.

Langston, C. A., 1981. Source inversion of seismic waveforms: the Konya India, earthquake of September 13, 1967, *Bull. Seism. Soc. Am.*, **71**, 1-24.

Langston, C. A., and Helmberger, D. V., 1975. A procedure for modeling shallow dislocation sources, *Geophys. J. R. astr. Soc.*, **42**, 117-130.

Lipman, S. C., Strobel, C. J., and Gulati, M. S., 1978. Reservoir performance of The Geysers field, *in, Proceedings of the Larderello workshop on geothermal resource assessment and reservoir engineering, Sept. 12-16, 1977, Pisa, Italy, Geothermics*, **7**, 209-219.

Ludwin, R. S., Cagnetti, V., and Bufe, C. G., 1982. Comparison of seismicity in The Geysers geothermal area with the surrounding region, *Bull. Seism. Soc. Am.*, **72**, 863-871.

Majer, E. L., and McEvilly, T. V., 1979. Seismological investigations at The Geysers geothermal field, *Geophysics*, **44**, 246-269.

McKenzie, D. P., 1969. The relationship between fault plane solutions for earthquakes and the direction of principal stresses, *Bull. Seism. Soc. Am.*, **59,** 591-601.

Michael, A. J., 1987. Use of focal mechanisms to determine stress: A control study, *J. Geophys. Res.*, **92,** 357-368.

O'Connell, D. R., 1986. Seismic velocity structure and microearthquake source properties at The Geysers, California, geothermal area, *Ph.D. Dissertation*, University of California, Berkeley, California.

Oldenburg, D. W., 1982. Multichannel appraisal deconvolution, *Geophys. J. R. astr. Soc.*, **69,** 405-414.

Oppenheimer, D. H., 1986. Extensional tectonics at The Geysers geothermal area, California, *J. Geophys. Res.*, **91,** 11463-11476.

Prescott, W. H., and Yu, S. B., 1986. Geodetic measurement of horizontal deformation in the northern San Francisco Bay region, California, *J. Geophys. Res.*, **91,** 7475-7484.

Saikia, C. K., and Herrmann, R. B., 1986. Moment-tensor solutions for three 1982 Arkansas swarm earthquakes by waveform modeling, *Bull. Seism. Soc. Am.*, **76,** 709-723.

Sipkin, S. A., 1982. Estimation of earthquake source parameters by the inversion of waveform data: synthetic waveforms, *Phys. Earth Planet. Int.*, **30,** 242-259.

Sipkin, S. A., 1986. Interpretation of non-double-couple earthquake mechanisms derived from moment tensor inversion, *J. Geophys. Res.*, **91,** 531-547.

Stump, B. W. and L. R. Johnson, 1977. The determination of source properties by the linear inversion of seismograms, *Bull. Seism. Soc. Am.*, **67**, 1489-1502.

Stump, B. W., and Johnson, L. R., 1984. Near-field source characterization of contained nuclear explosions in tuff, *Bull. Seism. Soc. Am.*, **74**, 1-26.

Professor Keiiti Aki
Center for Earth Sciences
University of Southern California
University Park
Los Angeles, CA 90089-0741

Professor Charles B. Archambeau
Cooperative Institute for Resch
  in Environmental Sciences
University of Colorado
Boulder, CO 80309

Dr. Thomas C. Bache Jr.
Science Applications Int'l Corp.
10210 Campus Point Drive
San Diego, CA 92121   (2 copies)

Dr. Douglas R. Baumgardt
Signal Analysis & Systems Div.
ENSCO, Inc.
5400 Port Royal Road
Springfield, VA 22151-2388

Dr. S. Bratt
Science Applications Int'l Corp.
10210 Campus Point Drive
San Diego, CA 92121

Dr. Lawrence J. Burdick
Woodward-Clyde Consultants
P.O. Box 93245
Pasadena, CA 91109-3245 (2 copies)

Professor Robert W. Clayton
Seismological Laboratory/Div. of
  Geological & Planetary Sciences
California Institute of Technology
Pasadena, CA 91125

Dr. Vernon F. Cormier
Department of Geology & Geophysics
U-45, Room 207
The University of Connecticut
Storrs, Connecticut 06268

Dr. Zoltan A. Der
ENSCO, Inc.
5400 Port Royal Road
Springfield, VA 22151-2338

Professor John Ferguson
Center for Lithospheric Studies
The University of Texas at Dallas
P.O. Box 830688
Richardson, TX 75083-0688

Professor Stanley Flatte'
Applied Sciences Building
University of California, Santa Cruz
Santa Cruz, CA 95064

Professor Steven Grand
Department of Geology
245 Natural History Building
1301 West Green Street
Urbana, IL 61801

Professor Roy Greenfield
Geosciences Department
403 Deike Building
The Pennsylvania State University
University Park, PA 16802

Professor David G. Harkrider
Seismological Laboratory
Div of Geological & Planetary Sciences
California Institute of Technology
Pasadena, CA 91125

Professor Donald V. Helmberger
Seismological Laboratory
Div of Geological & Planetary Sciences
California Institute of Technology
Pasadena, CA 91125

Professor Eugene Herrin
Institute for the Study of Earth
 & Man/Geophysical Laboratory
Southern Methodist University
Dallas, TX 75275

Professor Robert B. Herrmann
Department of Earth & Atmospheric
      Sciences
Saint Louis University
Saint Louis, MO 63156

Professor Lane R. Johnson
Seismographic Station
University of California
Berkeley, CA 94720

Professor Thomas H. Jordan
Department of Earth, Atmospheric
 and Planetary Sciences
Mass Institute of Technology
Cambridge, MA 02139

Dr. Alan Kafka
Department of Geology &
  Geophysics
Boston College
Chestnut Hill, MA 02167

Professor Leon Knopoff
University of California
Institute of Geophysics
 & Planetary Physics
Los Angeles, CA 90024

Professor Charles A. Langston
Geosciences Department
403 Deike Building
The Pennsylvania State University
University Park, PA 16802

Professor Thorne Lay
Department of Geological Sciences
1006 C.C. Little Building
University of Michigan
Ann Harbor, MI 48109-1063

Dr. Randolph Martin III
New England Research, Inc.
P.O. Box 857
Norwich, VT 05055

Dr. Gary McCartor
Mission Research Corp.
735 State Street
P.O. Drawer 719
Santa Barbara, CA 93102   (2 copies)

Professor Thomas V. McEvilly
Seismographic Station
University of California
Berkeley, CA 94720

Dr. Keith L. McLaughlin
S-CUBED,
A Division of Maxwell Laboratory
P.O. Box 1620
La Jolla, CA 92038-1620

Professor William Menke
Lamont-Doherty Geological Observatory
 of Columbia University
Palisades, NY 10964

Professor Brian J. Mitchell
Department of Earth & Atmospheric
      Sciences
Saint Louis University
Saint Louis, MO 63156

Dr. Jack Murphy
S-CUBED
A Division of Maxwell Laboratory
11800 Sunrise Valley Drive
Suite 1212
Reston, VA 22091 (2 copies)

Professor J. A. Orcutt
Institute of Geophysics and Planetary
   Physics, A-205
Scripps Institute of Oceanography
Univ. of California, San Diego
La Jolla, CA 92093

Professor Keith Priestley
University of Nevada
Mackay School of Mines
Reno, NV 89557

Jilmer Rivers
Teledyne Geotech
314 Montgomery Street
Alexandria, VA 22314

Professor Charles G. Sammis
Center for Earth Sciences
University of Southern California
University Park
Los Angeles, CA 90089-0741

Dr. Jeffrey L. Stevens
S-CUBED,
A Division of Maxwell Laboratory
P.O. Box 1620
La Jolla, CA 92038-1620

Professor Brian Stump
Institute for the Study of Earth & Man
Geophysical Laboratory
Southern Methodist University
Dallas, TX 75275

Professor Ta-liang Teng
Center for Earth Sciences
University of Southern California
University Park
Los Angeles, CA 90089-0741

Professor M. Nafi Toksoz
Earth Resources Lab
Dept of Earth, Atmospheric and
    Planetary Sciences
Massachusetts Institute of Technology
42 Carleton Street
Cambridge, MA 02142

Professor Terry C. Wallace
Department of Geosciences
Building #11
University of Arizona
Tucson, AZ 85721

Weidlinger Associates
ATTN: Dr. Gregory Wojcik
620 Hansen Way, Suite 100
Palo Alto, CA 94304

Professor Francis T. Wu
Department of Geological Sciences
State University of New York
At Binghamton
Vestal, NY 13901

Professor Francis T. Wu
Department of Geological Sciences
State University of New York
At Binghamton
Vestal, NY 13901

OTHERS (United States)

Dr. Monem Abdel-Gawad
Rockwell Internat'l Science Center
1049 Camino Dos Rios
Thousand Oaks, CA 91360

Professor Shelton S. Alexander
Geosciences Department
403 Deike Building
The Pennsylvania State University
University Park, PA 16802

Dr. Ralph Archuleta
Department of Geological
   Sciences
Univ. of California at
   Santa Barbara
Santa Barbara, CA

Dr. Muawia Barazangi
Geological Sciences
Cornell University
Ithaca, NY 14853

J. Barker
Department of Geological Sciences
State University of New York
  at Binghamton
Vestal, NY 13901

Mr. William J. Best
957 Westwood Drive
Vienna, VA 22180

Dr. A. Biswas
Geophysical Institute
University of Alaska
Fairbanks, AK 99701

Dr. G. A. Bollinger
Department of Geological Sciences
Virginia Polytechnical Institute
2044 Derring Hall
Blacksburg, VA 24061

Dr. James Bulau
Rockwell Int'l Science Center
1049 Camino Dos Rios
P.O. Box 1085
Thousand Oaks, CA 91360

Mr. Roy Burger
1221 Serry Rd.
Schenectady, NY 12309

Dr. Robert Burridge
Schlumberger-Doll Resch Ctr.
Old Quarry Road
Ridgefield, CT 06877

Science Horizons, Inc.
ATTN: Dr. Theodore Cherry
710 Encinitas Blvd., Suite 101
Encinitas, CA 92024 (2 copies)

Professor Jon F. Claerbout
Professor Amos Nur
Dept. of Geophysics
Stanford University
Stanford, CA 94305 (2 copies)

Dr. Anton W. Dainty
AFGL/LWH
Hanscom AFB, MA 01731

Dr. Steven Day
Dept. of Geological Sciences
San Diego State U.
San Diego, CA 92182

Professor Adam Dziewonski
Hoffman Laboratory
Harvard University
20 Oxford St.
Cambridge, MA 02138

Professor John Ebel
Dept of Geology & Geophysics
Boston College
Chestnut Hill, MA 02167

Dr. Alexander Florence
SRI International
333 Ravenswood Avenue
Menlo Park, CA 94025-3493

Dr. Donald Forsyth
Dept. of Geological Sciences
Brown University
Providence, RI 02912

Dr. Anthony Gangi
Texas A&M University
Department of Geophysics
College Station, TX 77843

Dr. Freeman Gilbert
Institute of Geophysics &
    Planetary Physics
Univ. of California, San Diego
P.O. Box 109
La Jolla, CA 92037

Mr. Edward Giller
Pacific Sierra Research Corp.
1401 Wilson Boulevard
Arlington, VA 22209

Dr. Jeffrey W. Given
Sierra Geophysics
11255 Kirkland Way
Kirkland, WA 98033

Dr. Henry L. Gray
Associate Dean of Dedman College
Department of Statistical Sciences
Southern Methodist University
Dallas, TX 75275

Rong Song Jih
Teledyne Geotech
314 Montgomery Street
Alexandria, Virginia 22314

Professor F.K. Lamb
University of Illinois at
  Urbana-Champaign
Department of Physics
1110 West Green Street
Urbana, IL 61801

Dr. Arthur Lerner-Lam
Lamont-Doherty Geological Observatory
 of Columbia University
Palisades, NY 10964

Dr. L. Timothy Long
School of Geophysical Sciences
Georgia Institute of Technology
Atlanta, GA 30332

Dr. Peter Malin
University of California at Santa Barbara
Institute for Central Studies
Santa Barbara, CA 93106

Dr. George R. Mellman
Sierra Geophysics
11255 Kirkland Way
Kirkland, WA 98033

Dr. Bernard Minster
Institute of Geophysics and Planetary
  Physics, A-205
Scripps Institute of Oceanography
Univ. of California, San Diego
La Jolla, CA 92093

Professor John Nabelek
College of Oceanography
Oregon State University
Corvallis, OR 97331

Dr. Geza Nagy
U. California, San Diego
Dept of Ames, M.S. B-010
La Jolla, CA 92093

Dr. Jack Oliver
Department of Geology
Cornell University
Ithaca, NY 14850

Dr. Robert Phinney/Dr. F.A. Dahlen
Dept of Geological
  Geophysical Sci. University
Princeton University
Princeton, NJ 08540 (2 copies)

RADIX Systems, Inc.
Attn: Dr. Jay Pulli
2 Taft Court, Suite 203
Rockville, Maryland 20850

Professor Paul G. Richards
Lamont-Doherty Geological
  Observatory of Columbia Univ.
Palisades, NY 10964

Dr. Norton Rimer
S-CUBED
A Division of Maxwell Laboratory
P.O. 1620
La Jolla, CA 92038-1620

Professor Larry J. Ruff
Department of Geological Sciences
1006 C.C. Little Building
University of Michigan
Ann Arbor, MI 48109-1063

Dr. Alan S. Ryall, Jr.
Center of Seismic Studies
1300 North 17th Street
Suite 1450
Arlington, VA 22209-2308   (4 copies)

Dr. Richard Sailor
TASC Inc.
55 Walkers Brook Drive
Reading, MA 01867

Thomas J. Sereno, Jr.
Science Application Int'l Corp.
10210 Campus Point Drive
San Diego, CA 92121

Dr. David G. Simpson
Lamont-Doherty Geological Observ.
  of Columbia University
Palisades, NY 10964

Dr. Bob Smith
Department of Geophysics
University of Utah
1400 East 2nd South
Salt Lake City, UT 84112

Dr. S. W. Smith
Geophysics Program
University of Washington
Seattle, WA 98195

Dr. Stewart Smith
IRIS Inc.
1616 N. Fort Myer Drive
Suite 1440
Arlington, VA 22209

Roudout Associates
ATTN: Dr. George Sutton,
Dr. Jerry Carter, Dr. Paul Pomeroy
P.O. Box 224
Stone Ridge, NY 12484 (4 copies)

Dr. L. Sykes
Lamont Doherty Geological Observ.
Columbia University
Palisades, NY 10964

Dr. Pradeep Talwani
Department of Geological Sciences
University of South Carolina
Columbia, SC 29208

Dr. R. B. Tittmann
Rockwell International Science Center
1049 Camino Dos Rios
P.O. Box 1085
Thousand Oaks, CA 91360

Professor John H. Woodhouse
Hoffman Laboratory
Harvard University
20 Oxford St.
Cambridge, MA 02138

Dr. Gregory B. Young
ENSCO, Inc.
5400 Port Royal Road
Springfield, VA 22151-2388

Dr. Peter Basham
Earth Physics Branch
Geological Survey of Canada
1 Observatory Crescent
Ottawa, Ontario
CANADA K1A 0Y3

Dr. Eduard Berg
Institute of Geophysics
University of Hawaii
Honolulu, HI 96822

Dr. Michel Bouchon - Universite
   Scientifique et Medicale de Grenob
Lab de Geophysique - Interne et
   Tectonophysique - I.R.I.G.M-B.P.
38402 St. Martin D'Heres
Cedex FRANCE

Dr. Hilmar Bungum/NTNF/NORSAR
P.O. Box 51
Norwegian Council of Science,
Industry and Research, NORSAR
N-2007 Kjeller, NORWAY

Dr. Michel Campillo
I.R.I.G.M.-B.P. 68
38402 St. Martin D'Heres
Cedex, FRANCE

Dr. Kin-Yip Chun
Geophysics Division
Physics Department
University of Toronto
Ontario, CANADA M5S 1A7

Dr. Alan Douglas
Ministry of Defense
Blacknest, Brimpton,
 Reading RG7-4RS
UNITED KINGDOM

Dr. Manfred Henger
Fed. Inst. For Geosciences & Nat'l Res.
Postfach 510153
D-3000 Hannover 51
FEDERAL REPUBLIC OF GERMANY

Dr. E. Husebye
NTNF/NORSAR
Post Box 51
N-2007 Kjeller, NORWAY

11

Ms. Eva Johannisson
Senior Research Officer
National Defense Research Inst.
P.O. Box 27322
S-102 54 Stockholm
SWEDEN

Tormod Kvaerna
NTNF/NORSAR
P.O. Box 51
N-2007 Kjeller, NORWAY

Mr. Peter Marshall, Procurement
 Executive, Ministry of Defense
Blacknest, Brimpton,
 Reading FG7-4RS
UNITED KINGDOM (3 copies)

Dr. Ben Menaheim
Weizman Institute of Science
Rehovot, ISRAEL 951729

Dr. Svein Mykkeltveit
NTNF/NORSAR
P.O. Box 51
N-2007 Kjeller, NORWAY (3 copies)

Dr. Robert North
Geophysics Division
Geological Survey of Canada
1 Observatory crescent
Ottawa, Ontario
CANADA, K1A 0Y3

Dr. Frode Ringdal
NTNF/NORSAR
P.O. Box 51
N-2007 Kjeller, NORWAY

Dr. Jorg Schlittenhardt
Federal Inst. for Geosciences & Nat'l Res.
Postfach 510153
D-3000 Hannover 51
FEDERAL REPUBLIC OF GERMANY

University of Hawaii
Institute of Geophysics
ATTN: Dr. Daniel Walker
Honolulu, HI 96822

Dr. Ramon Cabre, S.J.
c/o Mr. Ralph Buck
Economic Consular
American Embassy
APO Miami, Florida 34032

Professor Peter Harjes
Institute for Geophysik
Rhur University/Bochum
P.O. Box 102148 4630 Bochum 1
FEDERAL REPUBLIC OF GERMANY

Professor Brian L.N. Kennett
Research School of Earth Sciences
Institute of Advanced Studies
G.P.O. Box 4
Canberra, 2601
AUSTRALIA

Dr. B. Massinon
Societe Radiomana
27, Rue Claude Bernard
75005 Paris, FRANCE   (2 copies)

Dr. Pierre Mechler
Societe Radiomana
27, Rue Claude Bernard
75005 Paris, FRANCE

Dr. Ralph Alewine III
DARPA/NMRO
1400 Wilson Boulevard
Arlington, VA 22209-2308

Dr. Peter Basham
Geological Survey of Canada
1 Observatory Crescent
Ottawa, Ontario
CANADA K1A 0Y3

Dr. Robert Blandford
DARPA/NMRO
1400 Wilson Boulevard
Arlington, VA 22209-2308

Sandia National Laboratory
ATTN: Dr. H. B. Durham
Albuquerque, NM 87185

Dr. Jack Evernden
USGS-Earthquake Studies
345 Middlefield Road
Menlo Park, CA 94025

U.S. Geological Survey
ATTN: Dr. T. Hanks
Nat'l Earthquake Resch Center
345 Middlefield Road
Menlo Park, CA 94025

Dr. James Hannon
Lawrence Livermore Nat'l Lab.
P.O. Box 808
Livermore, CA 94550

U.S. Arms Control & Disarm. Agency
ATTN: Dick Morrow
Washington, D.C. 20451

Paul Johnson
ESS-4, Mail Stop J979
Los Alamos National Laboratory
Los Alamos, NM 87545

Ms. Ann Kerr
DARPA/NMRO
1400 Wilson Boulevard
Arlington, VA 22209-2308

Dr. Max Koontz
US Dept of Energy/DP 331
Forrestal Building
1000 Independence Ave.
Washington, D.C. 20585

Dr. W. H. K. Lee
USGS
Office of Earthquakes, Volcanoes,
  & Engineering
Branch of Seismology
345 Middlefield Rd
Menlo Park, CA 94025

Dr. William Leith
USGS
Mail Stop 928
Reston, VA 22092

Dr. Richard Lewis
Dir. Earthquake Engineering and
  Geophysics
U.S. Army Corps of Engineers
Box 631
Vicksburg, MS 39180

Dr. Robert Masse'
Box 25046, Mail Stop 967
Denver Federal Center
Denver, Colorado 80225

A. Morrow
ACDA, VI
Room 5741
320 21st Street N.W.
Washington, D.C. 20451

Dr. Keith K. Nakanishi
Lawrence Livermore National Laboratory
P.O. Box 808, L-205
Livermore, CA 94550 (2 copies)

Dr. Carl Newton
Los Alamos National Lab.
P.O. Box 1663
Mail Stop C335, Group E553
Los Alamos, NM 87545

Dr. Kenneth H. Olsen
Los Alamos Scientific Lab.
Post Office Box 1663
Los Alamos, NM 87545

Howard J. Patton
Lawrence Livermore National Laboratory
P.O. Box 808, L-205
Livermore, CA 94550

Mr. Chris Paine
Office of Senator Kennedy
SR 315
United States Senate
Washington, D.C. 20510

AFOSR/NP
ATTN: Colonel Jerry J. Perrizo
Bldg 410
Bolling AFB, Wash D.C. 20332-6448

HQ AFTAC/TT
Attn: Dr. Frank F. Pilotte
Patrick AFB, Florida 32925-6001

Mr. Jack Rachlin
USGS - Geology, Rm 3 C136
Mail Stop 928 National Center
Reston, VA 22092

Robert Reinke
AFWL/NTESG
Kirtland AFB, NM 87117-6008

HQ AFTAC/TGR
Attn: Dr. George H. Rothe
Patrick AFB, Florida 32925-6001

Donald L. Springer
Lawrence Livermore National Laboratory
P.O. Box 808, L-205
Livermore, CA 94550

Dr. Lawrence Turnbull
OSWR/NED
Central Intelligence Agency
CIA, Room 5G48
Washington, D.C. 20505

Dr. Thomas Weaver
Los Alamos Scientific Laboratory
Los Alamos, NM 97544

AFGL/SULL
Research Library
Hanscom AFB, MA 01731-5000 (2 copies)

Secretary of the Air Force (SAFRD)
Washington, DC 20330
Office of the Secretary Defense
DDR & E
Washington, DC 20330

HQ DNA
ATTN: Technical Library
Washington, DC 20305

Director, Technical Information
DARPA
1400 Wilson Blvd.
Arlington, VA 22209

AFGL/XO
Hanscom AFB, MA 01731-5000

AFGL/LW
Hanscom AFB, MA 01731-5000

DARPA/PM
1400 Wilson Boulevard
Arlington, VA 22209

Defense Technical
 Information Center
Cameron Station
Alexandria, VA 22314
(5 copies)

Defense Intelligence Agency
Directorate for Scientific &
 Technical Intelligence
Washington, D.C. 20301

Defense Nuclear Agency/SPSS
ATTN: Dr. Michael Shore
6801 Telegraph Road
Alexandria, VA 22310

AFTAC/CA (STINFO)
Patrick AFB, FL 32925-6001

Dr. Gregory van der Vink
Congress of the United States
Office of Technology Assessment
Washington, D.C. 20510